Ultra-broadband tunable optical vortex sources
超広帯域波長可変光渦レーザー光源

January 2018

千葉大学大学院 融合科学研究科
情報科学専攻 画像マテリアルコース

荒木　隼悟

（千葉大学審査学位論文）

Ultra-broadband tunable optical vortex sources
超広帯域波長可変光渦レーザー光源

January 2018

千葉大学大学院 融合科学研究科
情報科学専攻 画像マテリアルコース

荒木　隼悟

Acknowledgements

I would like to thank all people who have supported and encouraged me during my doctoral study and also pushed me to go on to the doctoral program.

First of all, I'd like to express my heartfelt appreciation to my supervisor Prof. Takashige Omatsu. He has provided a large number of scientific knowledges of laser physics and suggestions for experiments based on his great research activities, which guided me to solve the problem and improve my skill. He has also showed me how researchers should be. Without his overwhelming supports, I could not have completed my Ph.D. program. I'm extremely proud that I could build my academic career under the leading person in the field of optical vortices.

I also have special thanks to Dr. Katsuhiko Miyamoto, gave me many experimental advices and techniques, and to Ms. Asako Tsukamoto, a group secretary, who supported my domestic and foreign research activities. Their daily assists were indispensable for my Ph.D. project.

I am also forever grateful to Prof. Hajime Sakata and Dr. Masahiro Tomiki, University of Shizuoka, who led me to the road of laser physics, for his kind guidance and support in the master's degree.

I'm further grateful to Dr. Yoshiko Arita, Dr. Hiromasa Niinomi, Dr. Jung-Chen Tung, Prof. Helen. M. Pask (Macquarie Univ.), Dr. Andrew. J. Lee (Macquarie Univ.), and Dr. Ran Li (Macquarie Univ.) for all their help and advice throughout my Ph.D. study.

I also thank Dr. Kohei Toyoda, Dr. Taximaiti Yusufu, Dr. Fuyuto Takahashi, and Dr. Aizitiaili Abulikemu for a lot of wonderful memories.

I would also like to thank a co-worker Yuta Sasaki, who has worked hard and encouraged each other. His attitude toward study inspired me many times over. A relationship with him is my treasure. Thanks a lot.

I must also thank Dr. Muneyuki Adachi and Mr. Tsuyoshi Yamada in my previous company. They pushed me to resign the company and enter the doctoral course. Without it, I would not be the person I am today.

Furthermore, special thanks have to go to optical parametric oscillator team, Kensuke Suzuki, Shigeki Nishida, Roukuya Mamuti, and Kana Ando. I cannot express my gratitude toward them enough. And, I am also grateful to the past and present members, Guzhalay Juma, Ablimit Ablez, Yoshihiro Nishigata, Jun-Hyung Lee, Ma Yuanyuan, Kai Izumisawa, Kazuki Sano, Shunsuke Toyoshima, Shogo Nakano, Keigo Masuda, Koki

Yamaguchi, Tomohito Yamasaki, Fukutaro Shiraishi, Takanori Kineduka, Jun Shibakawa, Tatsuyuki Sugimoto, Yuri Nakamura, Takahiro Miyakawa, Ayane Murakami, Shuta Kitade, Mirzat Polat, He Jiahuan, Mitsuki Ichijyo, Tatsuya Kitamuki, Chisa Koriyama, Ryo Shinozaki, Ryosuke Nakamura, Kenshiro Niinuma, Masaki Furuta, Reimon Matsuo, Sung-Joo Kim, Michael Tomoki Horikawa, Masashi Abe, Azusa Ogawa, Maya Kowa, Honami Fujiwara, Yuji Miyamoto, Takayoshi Yano, Itsuki Yoshida, Manabu Magarisawa,

As the end of acknowledgements, I would like to thank my family for their dedicated supports to complete my research.

Abstract

This thesis presents the ultra-broadband tunable optical vortex sources in the visible to mid-infrared region. Recently, the structured light with spiral wavefront and orbital angular momentum (OAM), i.e. optical vortex, has been utilized in a large variety of laser applications, such as high-capacity optical telecommunications, super resolution microscope, and chiral structures fabrication. Wavelength-tunable optical vortex sources are required for the aforementioned applications.

In my doctoral program, I researched the extension of the wavelength/OAM-versatility of the optical vortex generated from an optical vortex pumped optical parametric oscillator, and a difference frequency generator pumped by the optical parametric oscillator.

At first, I demonstrated the tunable optical vortex laser with ultra-broadband tunability of over 2-octave band, by employing the optical vortex pumped optical parametric oscillation system using the diode-pumped laser as well as the non-critical phase-matching LiB_3O_5 crystal. Optical vortex output with a pulse energy of > 0.1 mJ (Maximum, 2.9 mJ) was obtained in a wavelength range of 0.67 to 2.57 μm, corresponding to a whole wavelength range that the LiB_3O_5 crystal allows for the non-critical phase-matching. The OAM of the vortex output could be also tuned within -1 to 2 (i.e. four OAM states).

Secondly, I present the ultra-widely tunable optical vortex generation in the mid-infrared region. By employing a $AgGaSe_2$ difference frequency generator pumped by a $KTiOPO_4$ optical vortex parametric oscillator, the tunability of 6-18 μm in which there are the eigen frequencies of bending and stretching modes for the various molecules was achieved.

Such broadband tunable optical vortex sources with OAM versatility will further accelerate the development of the new vortex applications in terms of material science.

Table of Contents

List of Figures

Chapter. 4

Chapter. 5

Chapter. 6

Chapter. 7

Appendix

Publications

[1] H. Nakagami, **S. Araki**, and H. Sakata, “Gain-switching pulse generation of Tm-doped fiber ring laser pumped with 1.6 μm laser diodes,” Laser Phys. Lett. **8**, 301 (2011).
[2] H. Sakata, **S. Araki**, R. Toyama, and M. Tomiki, “All-fiber Q-switched operation of thulium-doped silica fiber laser by piezoelectric microbending,” Appl. Opt. **51**, 1067 (2012).
[3] M. Ichikawa, **S. Araki**, and H. Sakata, “Wavelength control of Tm-doped fiber laser using nonidentical mechanical long-period fiber gratings,” Laser Phys. Lett. **10**, 025101 (2013).
[4] **S. Araki**, K. Kimpara, M. Tomiki, and H. Sakata, “Q-switched Tm-doped fiber lasers using dynamic microbends in oval-coating fibers,” Laser phys. **23**, 065102 (2013).
[5] T. Yusufu, Y. Sasaki, **S. Araki**, K. Miyamoto, and T. Omatsu, “Beam propagation of efficient frequency-doubled optical vortices,” Appl. Opt. **55**, 5263 (2016).
[6] A. Abulikemu, T. Yusufu, R. Mamuti, **S. Araki**, K. Miyamoto, and T. Omatsu, “Octave-band tunable optical vortex parametric oscillator,” Opt. Express **24**, 15204 (2016).
[7] **S. Araki**, K. Suzuki, S. Nishida, R. Mamuti, K. Miyamoto, and T. Omatsu, “Ultra-broadband tunable (0.67-2.57 μm) optical vortex parametric oscillator,” Jpn. J. Appl. Phys. **56**, 102701 (2017).
[8] **S. Araki**, K. Ando, K. Miyamoto, and T. Omatsu, “Ultra-widely tunable mid-infrared (6-18 μm) optical vortex source,” Appl. Opt. 57, 620 (2018).

International conferences

[1] **S. Araki**, R. Li, A. J. Lee, H. M. Pask, and T. Omatsu, "Q-switched self-Raman vortex laser using a defect mirror," The Conference on Lasers and Electro-Optics and the European Quantum Electronic Conference (CLEO®/Europe-EQEC, 2017), Munich, Germany, 25-29 June, 2017.

[2] **S. Araki**, K. Suzuki, S. Nishida, R. Mamuti, K. Miyamoto, and T. Omatsu, "Millijoule-level, ultra-broadband tunable (0.67-2.4 μm) optical vortex parametric laser," The Conference on Lasers and Electro-Optics and the European Quantum Electronic Conference (CLEO®/Europe-EQEC, 2017), Munich, Germany, 25-29 June, 2017.

[3] **S. Araki**, K. Suzuki, S. Nishida, K. Miyamoto, and T. Omatsu, "Widely tunable optical vortex parametric laser with versatility of orbital angular momentum," The Advanced Solid State Lasers Conference and Laser Applications Conference (ASSL/LAC, 2017), Nagoya, Japan, 1-5 Oct, 2017.

Chapter 1 – Optical vortices

1.1 What is optical vortices?

In 1992, Allen et.al. proposed that optical vortex with a doughnut-shaped spatial form owing to its helical wavefront, e.g. Laguerre-Gaussian laser mode, possesses an orbital angular momentum (OAM) assigned by an azimuthal quantum number, ℓ, termed as topological charge.[1)] To date, the optical vortex has been intensely studied in diverse fields, including laser trapping and manipulation (Fig. 1.2),[2,3)] materials processing, spatial division multiplexing optical telecommunications with large data capacities (Fig. 1.3),[4,5)] high spatial resolution scanning fluorescence microscopes (Fig. 1.4),[6,7)] nonlinear spectroscopies[8)] and so on.

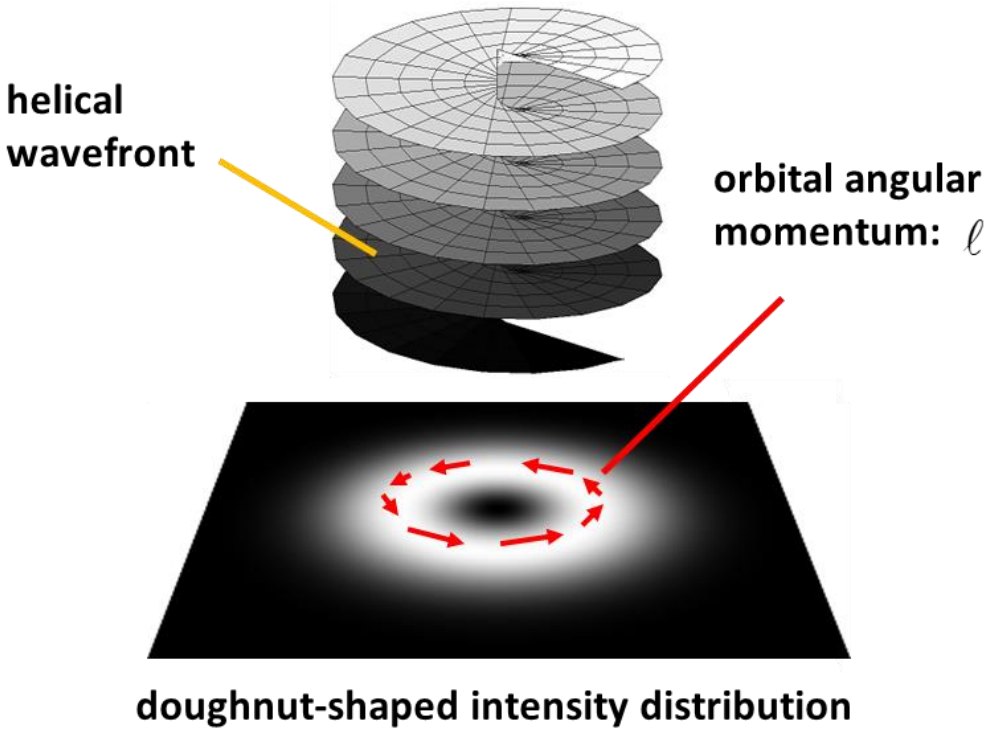

Fig. 1.1 Characteristics of optical vortex.

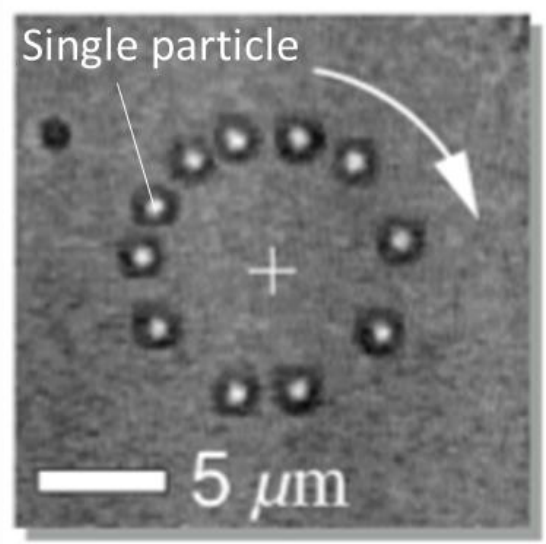

Fig. 1.2 Time-lapse image of a single colloidal sphere.[2] Optical vortex traps a submicron particle to be a ring and it forces the orbital motion.

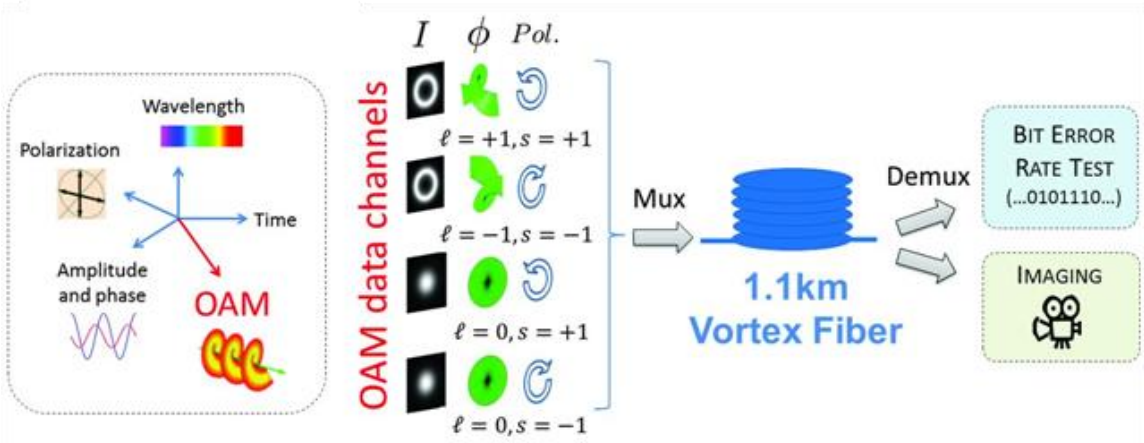

Fig. 1.3 Terabit scale large capacities optical telecommunication with the optical vortex beams.[5] Information multiplexing system based on the combination of the orbital angular momentum and the spin angular momentum (i.e. circularly polarization) by use of the vortex fiber, in which the refractive index profiles are designed to propagate stably for the 1st-order asymmetry modes.

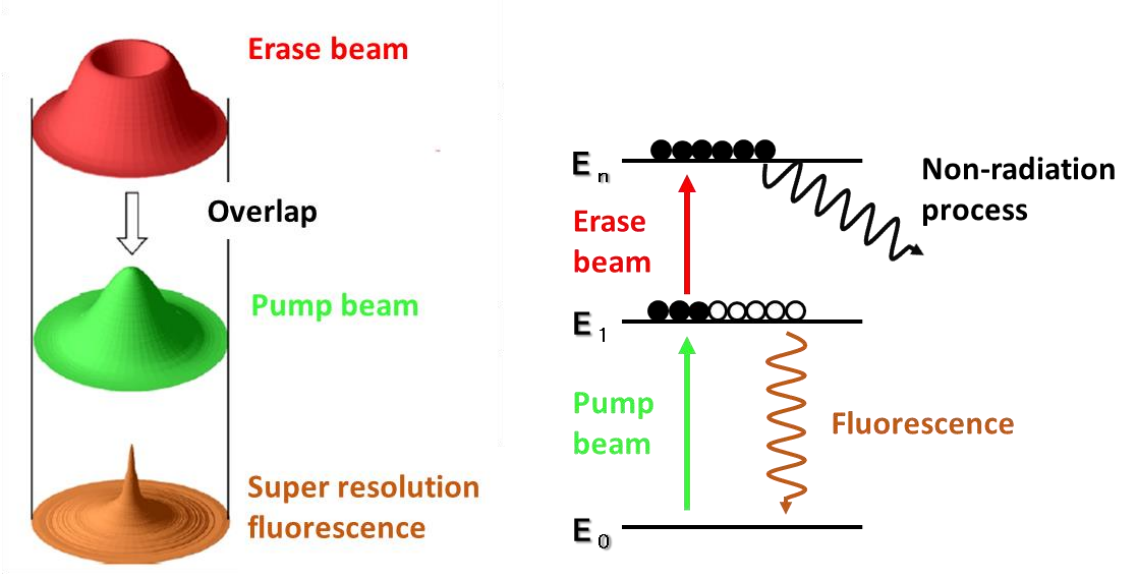

Fig.1.4 Schematic of super spatial resolution microscopies.[6)] Optical vortex beam with annular intensity profile is utilized for the quenching the fluorescence from the materials (stimulated emission depletion), which enables us to observe the materials with the spatial resolution beyond the diffraction limit.

In particular, materials microfabrication by optical vortex illumination provides us a variety of chiral structured materials. For instance, Toyoda et al. discovered that OAM can twist a metal (tantalum) to establish a chiral needle with a nano-scale tip diameter. Also, they found that the chirality of the structured needle is fully assigned by the handedness (sign of the topological charge) of the irradiated optical vortex beam (Fig. 1.5).[9,10)] The OAM further enables us to create chiral silicon structures[11)] and chiral organic surface reliefs[12)] (Fig. 1.6). Such chiral structured materials fabricated by the optical vortex illumination will be potentially applied to develop the new functional devices, for instance, biomedical MEMS,[13)] plasmonic metasurfaces,[14)] etc.

Above-mentioned applications require strongly the wavelength-diversity of optical vortices, whose wavelengths meet a specific absorption band of target material. To date, several researchers have successfully demonstrated nonlinear frequency conversion of the optical vortices, such as second harmonic generation,[15,16)] sum frequency mixing,[17,18)] stimulated Raman scattering,[19,20)] etc. In particular, optical parametric oscillation[21,22)] will provide us to develop wavelength-tunable vortex sources.

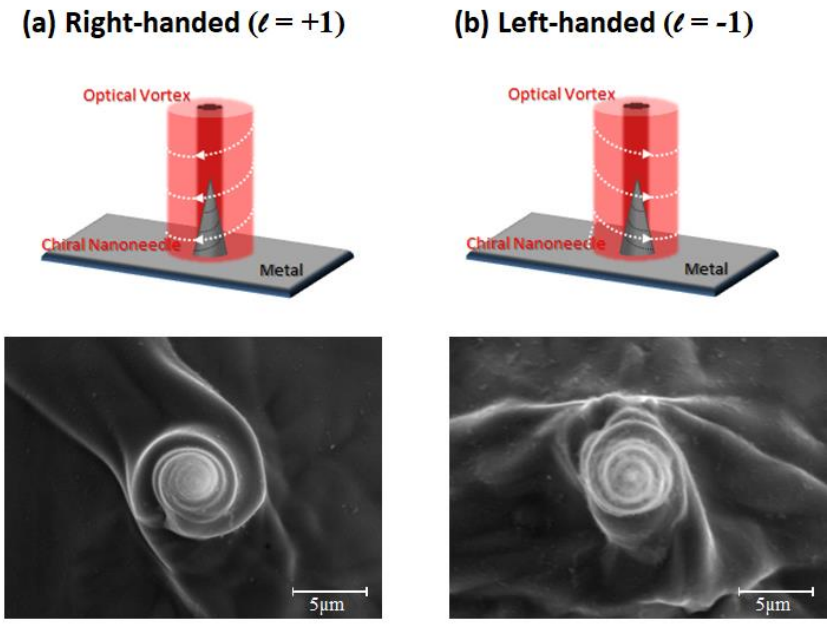

Fig. 1.5 Chiral metal nanoneedles formation on tantalum by optical vortices illumination.[9] If the handedness (sign of the topological charge) of the vortex beam is reversed, the spiral direction of the nanoneedle is inverted.

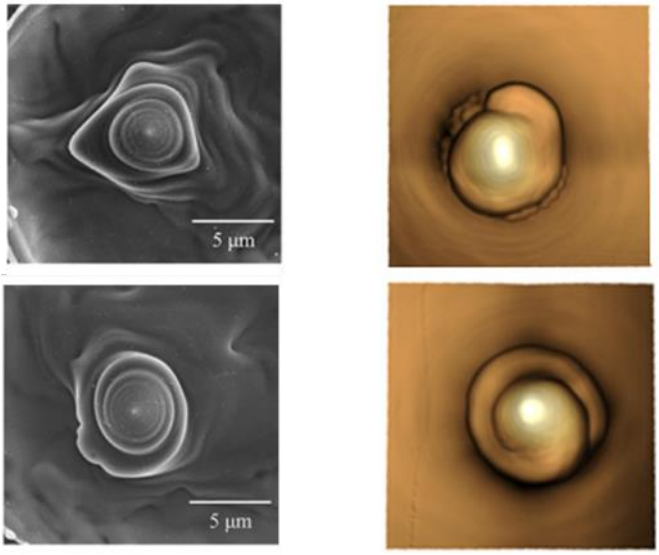

Fig. 1.6 Chiral structures in silicon (left side) and azo-polymer (right side).[11,12]

1.2 Thesis overview

In this thesis, I present wavelength-tunable optical vortex sources based on optical parametric oscillator, with an extremely wide tunability from visible to near-infrared region and in mid-infrared region, in which there are absorption bands of a variety of molecules (so-called “molecular finger print”). I have successfully demonstrated, for the first time, an ultra-broadband tunable (over 2-octave) optical vortex source based on a simple optical parametric oscillator with a single resonant cavity configuration. Furthermore, I report on a tunable optical vortex source in an entire mid-infrared region by employing a difference frequency generator pumped by optical parametric oscillator.

In chapter 2, I address the Laguerre-Gaussian modes, i.e. conventional optical vortices, and their theoretical formula including OAM.

Chapter 3 reviews several methods to generate the optical vortices, including a spiral phase plate, a spatial light modulator, and a stressed fiber.

In chapter 4, I also present fundamental theory of nonlinear frequency conversion processes based on 2^{nd}-order nonlinear phenomenon, including optical parametric amplification and oscillation.

In chapter 5, I report on an ultra-broadband (0.67-2.57 μm) tunable optical vortex source based on an optical vortex pumped LiB_3O_5 optical parametric oscillator. A basic concept of topological charge control in the optical parametric oscillator is also addressed.

In chapter 6, I demonstrate an ultra-widely tunable mid-infrared (6.0–18 μm) optical vortex source based on a $AgGaSe_2$ difference frequency generator pumped by optical vortex pumped $KTiOPO_4$ optical parametric oscillator.

Finally, I conclude my study and mention a prospective work of my thesis in chapter 7.

1.3 References

1) L. Allen, M. W. Beijersbergen, R. J. C. Spreeuw, and J. P. Woerdman, “Orbital angular momentum of light and the transformation of Laguerre-Gaussian laser modes,” Phys. Rev. A **45**, 8185 (1992).
2) J. E. Curtis, D. G. Grier, “Structure of Optical Vortices,” Phys. Rev. Lett. **90**, 133901(2003).
3) M. Padgett and R. Bowman, “Tweezers with a twist,” Nat. Photonics **5**, 343 (2011).
4) T. su, R. P. Scott, S. S. Djordjevic, N. K. Fontaine, D. J. Geisler, X. Cai, and S. J. B. Yoo,

"Demonstration of free space coherent optical communication using integrated silicon photonic orbital angular momentum devices," Opt. Express **20**, 9396 (2012).

5) N. Bozinovic, Y. Yue, Y. Ren, M. Tur, P. Kristensen, H. Huangr, A. E. Willner, and S. Ramachandran, "Terabit-scale orbital angular momentum mode division multiplexing in fibers," Science **340**, 1545 (2013).
6) T. Watanabe, Y. Iketaki, T. Omatsu, K. Yamamoto, S. Ishiuchi, M. Sakai, and M. Fujii, "Two-Color Far-Field Super-Resolution Microscope using a Doughnut Beam," Chem. Phys. Lett. **371**, 634 (2003).
7) S. Bretschneider, C. Eggeling, and S. W. Hell, "Breaking the diffraction barrier in fluorescence microscopy by optical shelving," Phys. Rev. Lett. **98**, 218103 (2007).
8) K. Shigematsu, Y. Toda, K. Yamane, and R. Morita, "Orbital angular momentum spectral dynamics of GaN excitons excited by optical vortices," Jpn. J. Appl. Phys. **52**, 08JL08 (2013).
9) K. Toyoda, K. Miyamoto, N. Aoki, R. Morita, and T. Omatsu, "Using optical vortex to control the chirality of twisted metal nanostructures," Nano Lett. **12**, 3645 (2012).
10) K. Toyoda, F. Takahashi, S. Takizawa, Y. Tokizane, K. Miyamoto, R. Morita, and T. Omatsu, "Transfer of light helicity to nanostructures," Phys. Rev. Lett. **110**, 143603 (2013).
11) F. Takahashi, S. Takizawa, H. Hidai, K. Miyamoto, R. Morita, and T. Omatsu, "Optical vortex illumination to create chiral monocrystalline silicon nanostructures," Physica Status Solidi (a) **213**, 1063 (2016).
12) M. Watabe, G. Juman, K. Miyamoto, and T. Omatsu, "Light induced conch-shaped relief in an azo-polymer film," Sci. Rep. **4**, 4281 (2014).
13) S. Khumpuang, M. Horade, K. Fujioka, and S. Sugiyama, "Microneedle fabrication using the plane pattern to cross-section transfer method," Smart Mater. Struct. **15**, 600 (2006).
14) V. K. Valev, J. J. Baumberg, C. Sibilia, T. Verbiest, "Chirality and chiroptical effects in plasmonic nanostructures: fundamentals, recent progress and outlooks," Adv. Mater. **25**, 2517 (2013).
15) K. Dholakia, N. B. Simpson, and M. J. Padgett, "Second-harmonic generation and the orbital angular momentum of light," Phys. Rev. A **54**, R3742 (1996).
16) J. Courtial, K. Dholakia, L. Allen, and M. J. Padgett, "Second-harmonic generation and the conservation of orbital angular momentum with high-order Laguerre-Gaussian modes," Phys. Rev. A **56**, 4193 (1997).
17) A. Brežanskis, A. Matijošius, A. Piskarskas, V. Smilgevičius, and A. Stabinis, "Sum-frequency mixing of optical vortices in nonlinear crystals," Opt. Commun. **150**, 372

(1998).
18) G. Shao, Z. Wu, J. Chen, F. Xu, and Y. Lu, “Nonlinear frequency conversion of fields with orbital angular momentum using quasi-phase-matching,” Phys. Rev. A **88**, 063827 (2013).
19) A. J. Lee, T. Omatsu, and H. M. Pask, “Direct generation of a first-Stokes vortex laser beam from a self-Raman laser,” Opt. Express **21**, 12401 (2013).
20) A. J. Lee, C. Zhang, T. Omatsu, and H. M. Pask, “An intracavity, frequency-doubled self-Raman vortex laser.” Opt. Express **22**, 5400 (2014).
21) K. Miyamoto, S. Miyagi, M. Yamada, K. Furuki, N. Aoki, M. Okida, and T. Omatsu, “Optical vortex pumped mid-infrared optical parametric oscillator,” Opt. Express **19**, 12220 (2011).
22) T. Yusufu, Y. Tokizane, M. Yamada, K. Miyamoto, and T. Omatsu, “Tunable 2-μm optical vortex parametric oscillator,” Opt. Express **20**, 23666 (2012).

Chapter 2 – Laguerre-Gaussian modes and orbital angular momentum

In this chapter, Laguerre-Gaussian modes, eigen solutions for the paraxial electromagnetic wave equation at a cylindrical coordinate, and their OAM are reviewed.

2.1 Laguerre-Gaussian modes

The electromagnetic wave equation from Maxwell's equations and materials equations is given by

$$\nabla^2 \boldsymbol{E} - \mu\varepsilon \frac{\partial^2}{\partial t^2} \boldsymbol{E} = 0, \tag{2.1}$$

where ε is the dielectric constant, and μ is the magnetic permeability, respectively. The electric field $\boldsymbol{E}$ is written by $\boldsymbol{E}(\boldsymbol{r}, t) = U(\boldsymbol{r})\exp(i\omega t)$, thus, the equation (2.1) can be expressed as follow:

$$(\nabla^2 + k^2)U(\boldsymbol{r}) = 0, \tag{2.2}$$

where k is wave number by $k^2 = \omega^2\mu\varepsilon(\boldsymbol{r})$. This formula is called as Helmholtz equation. When the wave $\boldsymbol{E}$ propagates along the z-axis, $U(\mathbf{r})$ must be written by

$$U(\boldsymbol{r}) = u(r, \phi, z)\exp(-ik_z z), \tag{2.3}$$

where $u(r, \phi, z)$ is the complex amplitude of the electric field in the cylindrical coordinate. And then, the following formula can be obtained by substituting eq. (2.3) for eq. (2.2):

$$\left(\frac{\partial^2}{\partial r^2} + \frac{1}{r}\frac{\partial}{\partial r} + \frac{1}{r^2}\frac{\partial^2}{\partial \phi^2} - 2ik_z\frac{\partial}{\partial z}\right)u(r, \phi, z) = 0. \tag{2.4}$$

In this case, the *slowly varying amplitude* (SVA) approximation, in which the variation of the amplitude is small enough to the propagation distance, is assumed below.

$$\frac{\partial^2}{\partial z^2} \ll k\frac{\partial}{\partial z}, \quad \frac{\partial^2}{\partial z^2} \ll k^2 u \tag{2.5}$$

The Laguerre-Gaussian (LG) modes, the eigen modes of eq. (2.4), are given as follows :

$$u_{p,\ell}(r,\phi,z) = C_{p,\ell}\frac{\omega_0}{\omega(z)}\left(\frac{\sqrt{2}\,r}{\omega(z)}\right)^{|\ell|} L_p^{|\ell|}\left(\frac{2r^2}{\omega^2(z)}\right)\cdot \exp(i\ell\phi) \\ \cdot \exp\left(-\frac{r^2}{\omega^2(z)} - ik\frac{r^2}{2R(z)} + i(2p+|\ell|+1)\eta(z)\right), \tag{2.6}$$

$$\omega^2(z) = \omega_0^2\left[1+\left(\frac{\lambda z}{\pi\omega_0^2}\right)^2\right], \tag{2.7}$$

$$R(z) = z\left[1+\left(\frac{\pi\omega_0^2}{\lambda z}\right)^2\right], \tag{2.8}$$

$$\eta(z) = \tan^{-1}\left(\frac{\lambda z}{\pi\omega_0^2}\right), \tag{2.9}$$

where $C_{p,\ell}$ is the normalized constant with radial and azimuthal indices p and ℓ, L_p^ℓ is the associated Laguerre polynomial, $\omega(z)$ is the mode size, ω_0 is the minimum beam waist at on $z = 0$, $R(z)$ is the curvature radius and $\eta(z)$ represents the Gouy phase, respectively. Some Laguerre polynomials are listed as follows:

$$L_0^\ell(x) = 1$$
$$L_1^\ell(x) = -x + (\ell+1)$$
$$L_2^\ell(x) = \frac{1}{2}[x^2 - 2(\ell+2)x + (\ell+1)(\ell+2)]$$

Also, the corresponding LG modes exhibit the spatial forms as shown in Fig. 2.1.

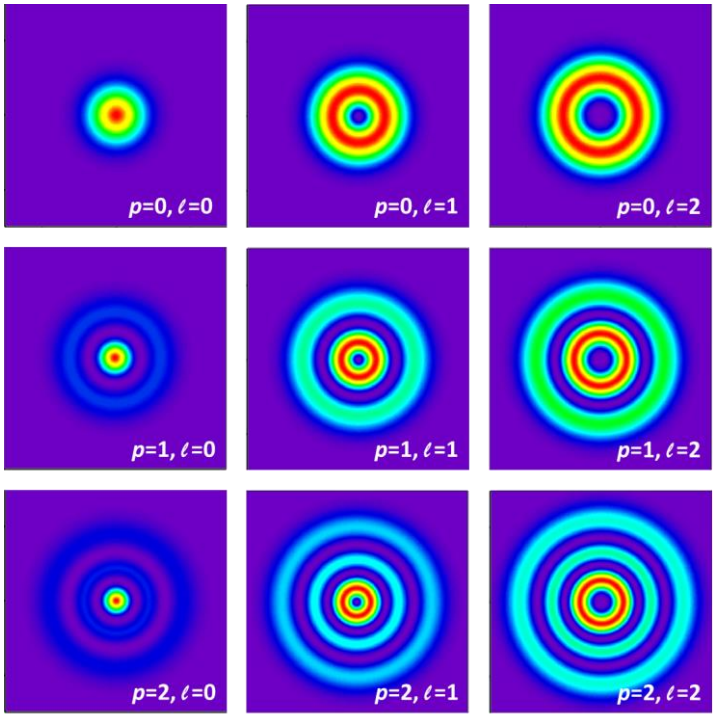

Fig. 2.1 Spatial forms of the Laguerre-Gaussian modes.

2.2 Orbital angular momentum (OAM)

Maxwell equations are rewritten by utilizing the vector potential $\boldsymbol{A}$ and scalar potential ϕ and providing the gauge transformation $[\boldsymbol{A}' = \boldsymbol{A} + \mathrm{grad}(\chi),\ \phi' = \phi - \partial\chi/\partial t]$ and the Lorentz condition, the electromagnetic equations are achieved by

$$\left(\Delta - \varepsilon\mu\frac{\partial^2}{\partial t^2}\right)\phi = 0, \tag{2.10}$$

$$\left(\Delta - \varepsilon\mu\frac{\partial^2}{\partial t^2}\right)\boldsymbol{A} = 0, \tag{2.11}$$

$$\nabla\cdot\boldsymbol{A} + \varepsilon\mu\frac{\partial\phi}{\partial t} = 0. \tag{2.12}$$

Defining $\boldsymbol{A}$ as $\boldsymbol{A} = \boldsymbol{n}u\exp(ikz)$, $\boldsymbol{E}$ and $\boldsymbol{B}$ can be derived as follows:

$$\boldsymbol{E} = i\omega\left[\boldsymbol{n}u + \frac{i}{k}\boldsymbol{e_z}(\boldsymbol{n}\cdot\nabla_T)u\right]\exp(ikz), \tag{2.13}$$

$$\boldsymbol{B} = ik\left(\boldsymbol{e_z}\times\boldsymbol{n}u + \frac{i}{k}\boldsymbol{n}\cdot\nabla_T u\right)\exp(ikz), \tag{2.14}$$

where $\boldsymbol{n}$ is $(\alpha\boldsymbol{e_x} + \beta\boldsymbol{e_y})\exp(-i\omega t)$, u is the complex amplitude, and ∇_T is $(\partial/\partial x)\boldsymbol{e_x} + (\partial/\partial \mathrm{y})\boldsymbol{e_y}$. The resulting Poynting vector, $\boldsymbol{S}$, should be expressed by

$$\begin{aligned}\boldsymbol{S} &= \frac{1}{2\mu}(\boldsymbol{E}^* \times \boldsymbol{B} + \boldsymbol{E} \times \boldsymbol{B}^*) \\ &= \frac{i\omega}{2\mu}(u\nabla_T u^* - u^*\nabla_T u) + \frac{\omega k}{\mu}|u|^2\boldsymbol{e_z},\end{aligned} \tag{2.15}$$

where the first term represents the energy flow associated with phase gradient in *xy*-plane, corresponding to the OAM.

Assuming $u \propto \exp(i\ell\phi)$, the OAM density, $\boldsymbol{l}$, is given as eq. (2.16).

$$\boldsymbol{l} = rp_\phi = \varepsilon\omega\ell|u|^2, \tag{2.16}$$

where $\boldsymbol{P} = p_r\boldsymbol{e_r} + p_\phi\boldsymbol{e_\phi} = 1/c^2\boldsymbol{S}$. The ratio of the OAM density to energy density is expressed by

$$\frac{\varepsilon\omega\ell|u|^2}{\varepsilon\omega^2|u|^2} = \frac{\ell}{\omega} = \ell\hbar/\omega\hbar, \tag{2.17}$$

indicating that optical vortex carries the OAM of $\ell\hbar$ per a photon.

Chapter 3 – Optical vortex generation

This chapter reviews several methods to generate the optical vortices, e.g. a spiral phase plate, a cylindrical lens pair, a stressed optical fiber etc.. In particular, the optical vortex generation based on the fiber technology is addressed in details.

3.1 Spiral phase plate and astigmatic mode converter

A spiral phase plate (SPP),[1,2] segmented along the azimuthal direction, provides a phase term of $\exp(i\ell\phi)$ to a plane wavefront:

$$u' = u\exp(i\ell\phi), \tag{3.1}$$

where u and u' is the electric field amplitude of the incident beam and the transformed beam, respectively. The thickness of the SPP is proportional to azimuthal angle ϕ (Fig. 3.1).

$$h = h_s\frac{\phi}{2\pi} + h_0, \tag{3.2}$$

where h_0 is the height of the base and h_s is the step height. The SPP must be designed for a specified wavelength λ. The resultant phase difference by the spiral phase plate is then given by

$$\Delta\psi = \frac{2\pi}{\lambda}\left[\frac{(n-n_0)h_s\cdot\phi}{2\pi}\right], \tag{3.3}$$

where n and n_0 are refractive indices of the plate and its surroundings. An azimuthal quantum number (so called topological charge), ℓ, corresponds to $(n-n_0)h_s/\lambda$.

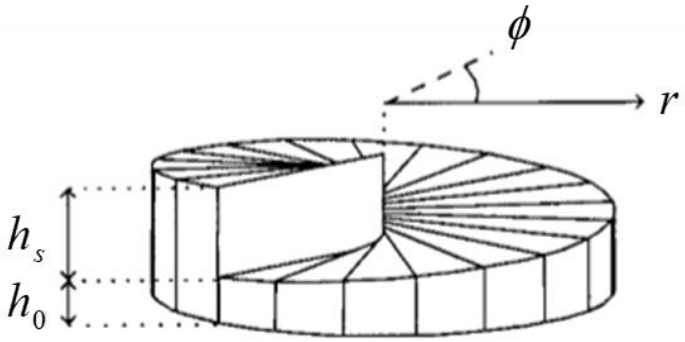

Fig. 3.1 Spiral phase plate.[1)]

A cylindrical lens pair acts as a mode conversion based on Gouy phase shift that focused laser beam experiences.[3,4] The $LG_{0,1}$ mode can be expressed by the superposition between $HG_{1,0}$ and $HG_{0,1}$ modes with $\pi/2$ phase shift. The focusing cylindrical lenses tilted 45 degree with respect to the optical axis yield the phase difference of $\pi/2$ between the $HG_{1,0}$ and $HG_{0,1}$ modes, thereby converting the tilted $HG_{1,0}$ ($HG_{0,1}$) mode to the $LG_{0,1}$ mode (Fig. 3.2).

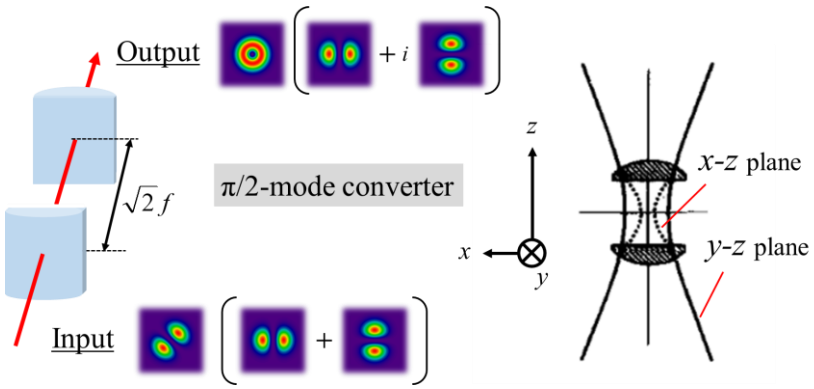

Fig. 3.2 Astigmatic laser mode converter.[3]

3.2 Stressed optical fiber

A Gaussian beam is also transformed into $LP_{1,1}$ mode, composed of orthogonal HG_{10} and HG_{01} modes by off-axially coupling into the few-mode fiber,[5,6] and it is further transformed into the $LG_{0,1}$ mode by appropriately applying stress to the fiber (Fig. 3.3) (stress-induced birefringence effect).

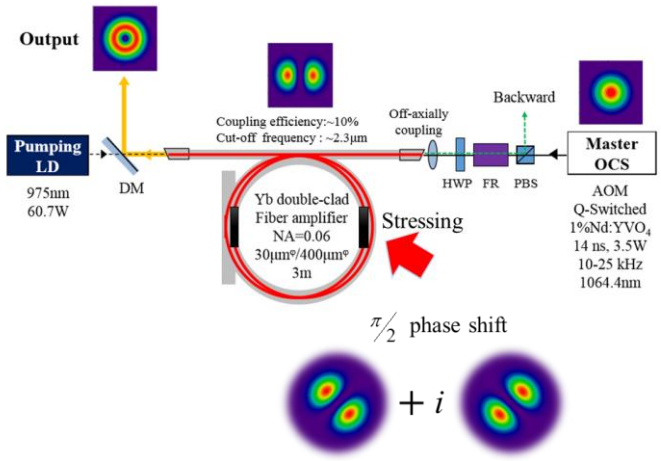

Fig. 3.3 Conversion to the vortex beam by stressed optical fiber.[6]

This stressed fiber configuration has been successfully demonstrated to generate efficiently the $LG_{0,1}$ mode in a visible and near-infrared region, and it will potentially be extended to develop 1.5 μm and 2 μm vortex sources based on erbium (Er) and thulium (Tm) doped fibers. In fact, a Q-switched Tm-doped fiber laser with a moderate pulse energy formed by all fiber components has been developed.[7,8)]

A schematic diagram of the Q-switched Tm-doped fiber laser is shown in Fig. 3.4. A thulium doped fiber with a length of 1.5 m was pumped by a 1.6 μm In-GaAsP laser diode via a variable-ratio coupler. A Q-switching device, i.e. loss modulator, was composed of electrically controlled piezoelectric actuators, modulating efficiently a radiation loss based on core-clad coupling [according to eq. (3.4)] as a quasi-fiber grating.

$$\beta_{core} - \beta_{clad} = \frac{2\pi}{\Lambda} \leftrightarrow \lambda_L = \Lambda\left(n_{core} - n_{clad}^{(m)}\right), \tag{3.4}$$

where β is the propagation constant including refractive index, and Λ is the spatial period of the grating, respectively. The dynamic fiber grating driven by the actuators forced the fiber laser to lase at Q-switch operation (Fig.3.5).

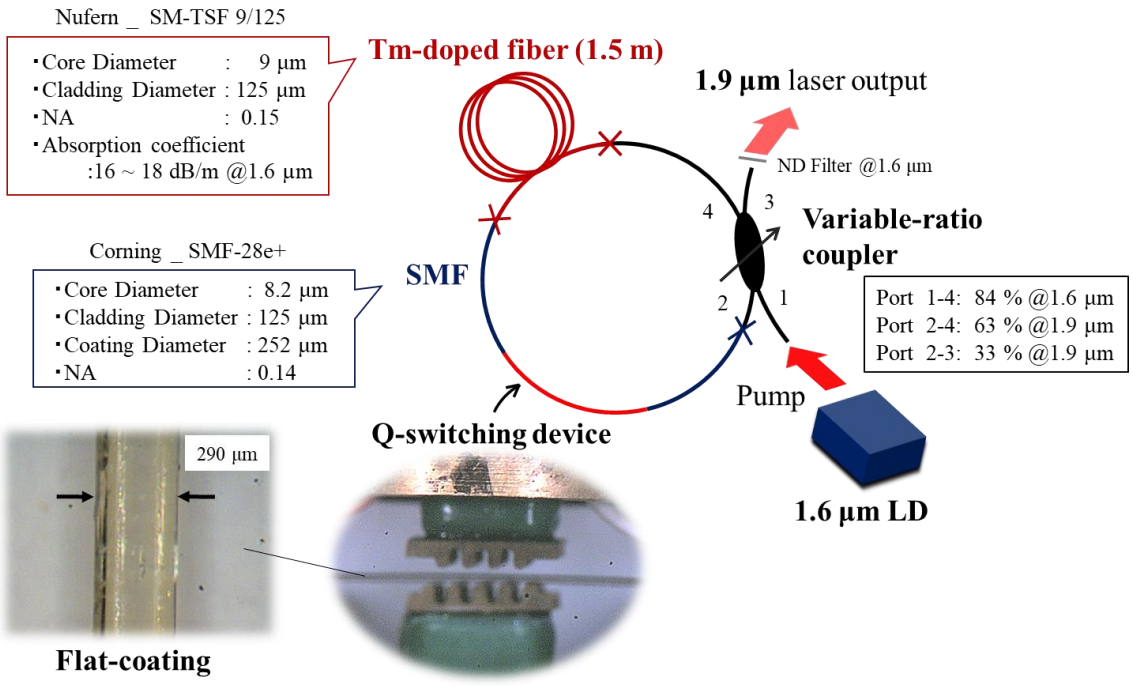

Fig. 3.4 All-fiber laser system for near-infrared radiation.[8)]

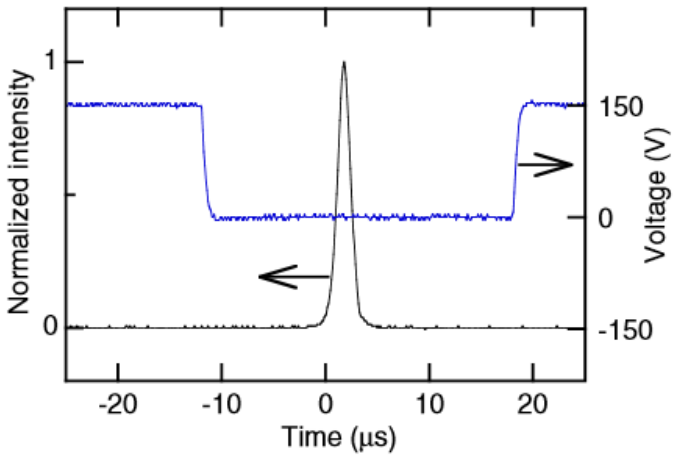

Fig. 3.5 Typical output laser pulse. Blue line shows driving voltage to the actuator.

The operation wavelength of the Tm-doped fiber laser could be also controlled by utilizing a mechanical fiber grating configuration with grating-period tunability [the schematic diagram is shown in Fig. 3.6(a)].[9] The fiber grating formed a band pass filter in the fiber ring cavity [Fig. 3.6(b)], resulting in controlling of laser gain. With this system, the tuning region of 1.87-1.97 μm was achieved by varying the grating period, as shown in Fig. 3.7. These laser systems will further be extended to develop tunable 2 μm vortex sources.

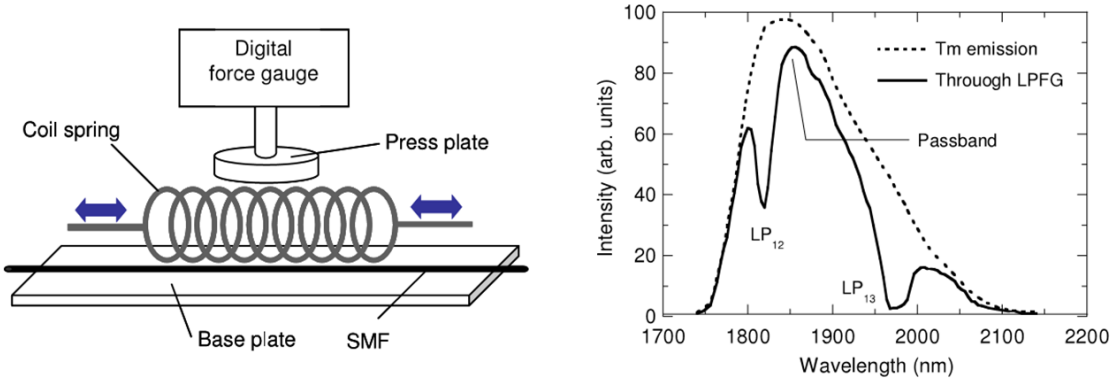

Fig. 3.6 (a) Schematic diagram of the mechanical fiber grating configuration and (b) Measured transmission spectrum of the fiber grating based on the spontaneous emission of the Tm-doped fiber.

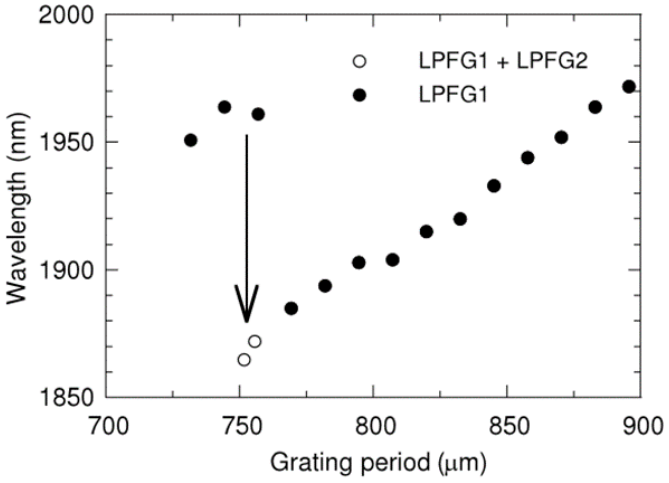

Fig. 3.7 Lasing wavelength as a function of fiber grating period.

3.3 References

1) M. W. Beijersbergen, R. P. C. Coerwinkel, M. Kristensen, and J. P. Woerdman, "Helical-wavefront laser beams produced with a spiral phaseplate," Opt. Commun. **112**, 321 (1994).
2) G. A. Turnbull, D. A. Robertson, G. M. Smith, L. Allen, and M. J. Padgett, "The generation of free-space Laguerre-Gaussian modes at millimetre-wave frequencies by use of a spiral phaseplate," Opt. Commun. **127**, 183 (1995).
3) M.W. Beijersbergen, L. Allen, H.E.L.O. van der Veen, and J.P. Woerdman, "Astigmatic laser mode converters and transfer of orbital angular momentum," Opt. Commun. **96**, 123 (1993).
4) M. Padgett, J. Alrlt, and N. Simpson, "An experiment to observe the intensity and phase structure of Laguerre-Gaussian laser modes," Am. J. Phys. **64**, 77 (1996).
5) Y. Tanaka, M. Okida, K. Miyamoto, and T. Omatsu, "High power picosecond vortex laser based on a large-mode-area fiber amplifier," Opt. Express **17**, 14362 (2009).
6) M. Koyama, T. Hirose, M. Okida, K. Miyamoto, and T. Omatsu, "Nanosecond vortex laser pulses with Millijoule pulse energies from a Yb-doped double-clad fiber power amplifier," Opt. Express **19**, 14420 (2011).
7) H. Sakata, S. Araki, R. Toyama, and M. Tomiki, "All-fiber Q-switched operation of thulium-doped silica fiber laser by piezoelectric microbending," Appl. Opt. **51**, 1067 (2012).

8) S. Araki, K. Kimpara, M. Tomiki, and H. Sakata, “Q-switched Tm-doped fiber lasers using dynamic microbends in oval-coating fibers,” Laser phys. **23**, 065102 (2013).
9) M. Ichikawa, S. Araki, and H. Sakata, “Wavelength control of Tm-doped fiber laser using nonidentical mechanical long-period fiber gratings,” Laser Phys. Lett. **10**, 025101 (2013).

Chapter 4 – Optical parametric oscillators

This chapter gives basic knowledges of frequency conversion based on a 2nd-order nonlinear optical effects, especially optical parametric process including generation, amplification, and oscillation.

4.1 Background

Optical parametric oscillators,[1)] based on second-order nonlinear optical process, allow us to develop wavelength-tunable sources in a visible and infrared region, thus, they play an important role in various applications, in particular, spectroscopy.

Light induced polarization P_i in the i-axis direction can be expressed as follows:

$$P_i = \varepsilon_0 \chi_{ij} E_j + \varepsilon_0 (\chi_{ijk}) E_j E_k + \varepsilon_0 (\chi_{ijkl}) E_j E_k E_l + \cdots, \qquad (4.1)$$

where subscripts (= i, j, k, l, ⋯) denote either axis of the x, y, and z, ε_0 is the dielectric constant in the vacuum, and χ is the electric susceptibility for the medium. The second term represents the second-order nonlinear polarization proportional to the square of the electric fields.

Figure 4.1 describes three photon interaction in this second-order nonlinear process, in which a high energy photon (ω_p, defined as the pump) breaks into two low energy photons (ω_s, ω_i, defined as the signal and the idler, respectively).

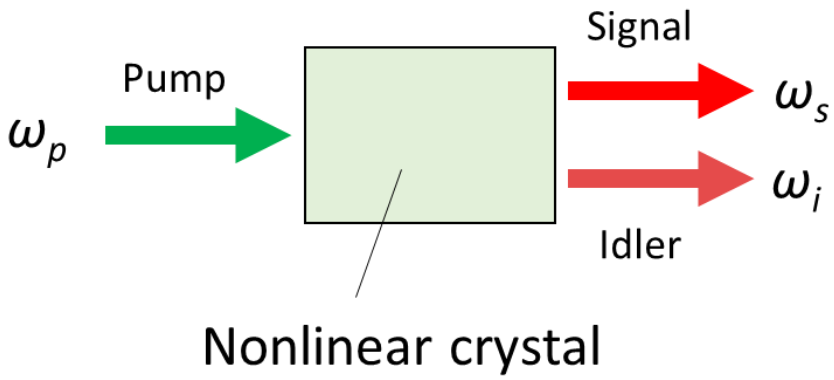

Fig. 4.1 diagram of the three photon optical parametric process.

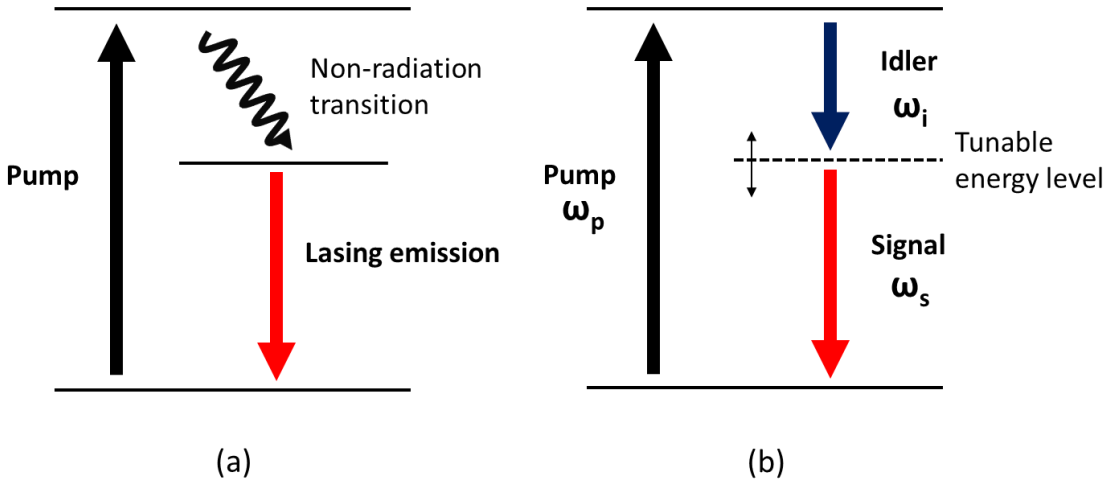

Fig. 4.2 the difference between (a) three-level laser and (b) three photon parametric process.

An energy conservation among three photons is always established, thus, ω_s (ω_i) can be varied in a frequency range of $0 - \omega_p$ ($\omega_p - 0$) [Fig. 4.2(b)], thereby yielding wavelength versatility in optical parametric process.

Frequencies of the signal and the idler are determined by momentum conservation among three photons, namely phase matching condition given by eq. (4.3).

$$\omega_p = \omega_s + \omega_i, \tag{4.2}$$

$$\boldsymbol{k}_p = \boldsymbol{k}_s + \boldsymbol{k}_i, \tag{4.3}$$

where, $k_\omega (= n_\omega \omega / c)$ is the wave number.

The phase matching condition is satisfied by utilizing wavelength dispersion of refractive index in an anisotropic crystal. In general, the anisotropic crystal exhibits birefringence for two orthogonal polarizations, i.e. ordinary and extraordinary polarizations. The refractive index n_e (θ) of extraordinary polarization varies by an incident angle θ with respect to a crystal orientation.

$$\frac{1}{n_e^2(\theta)} = \frac{\cos^2\theta}{n_o^2} + \frac{\sin^2\theta}{n_e^2}, \tag{4.4}$$

where n_o and n_e denote the refractive index at $\theta = 0°$ or $90°$, respectively. Figure 4.3 shows the diagram for Type-I phase matching in the negative crystal. Type-I phase matching indicates that the pump polarization is orthogonal to that of the signal and idler. Namely, if the pump polarization is extraordinary (ordinary), the signal and idler

polarizations are ordinary (extraordinary). In type-II phase matching, the resulting signal polarization is orthogonal to that of idler.

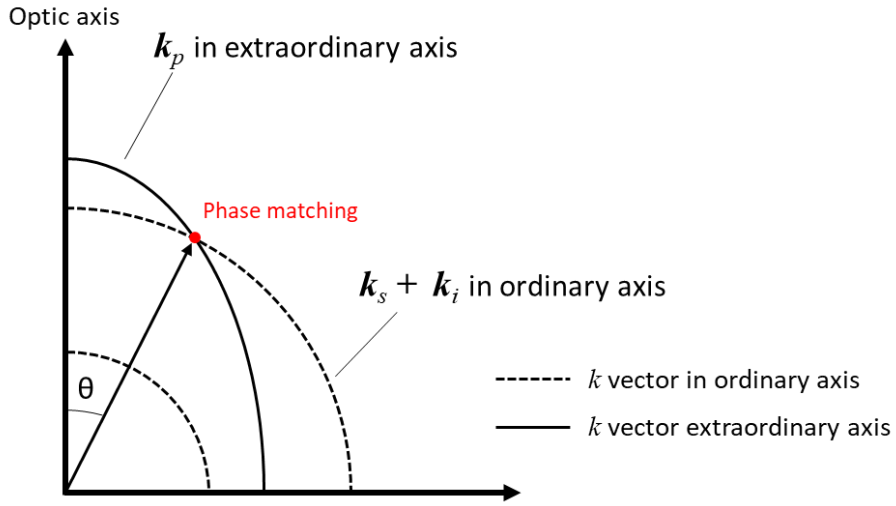

Fig. 4.3 Type-I phase matching by birefringence of the negative crystal.

Non-critical phase matching (NCPM) based on temperature control of the nonlinear crystal enables us to provide a wide acceptance of detuning angle among the pump, signal and idler without mechanical alignment of the crystal. The pump, signal and idler then propagate at $\theta = 0°$ and 90° of the crystal orientation, so as to minimize the walk-off effect.

4.2 Nonlinear crystal

[1] LiB_3O_5 (LBO)

A Lithium triborate (LiB_3O_5, LBO) (Fig. 4.4),[2-4] discovered and developed by Fujian Institute of Research on the structure of Matter (FIRSM), possesses extremely high transmission in a wavelength region of 160 - 2600 nm (as shown in Fig. 4.5). This crystal also exhibits small walk-off effects owing to its small birefringence. Thus, it allows us to establish the non-critical phase matching for the optical parametric oscillator (OPO) pumped by a conventional frequency-doubled Nd:YAG laser (532 nm). Furthermore, its relatively high optical damage threshold enables us to develop high power OPO system.

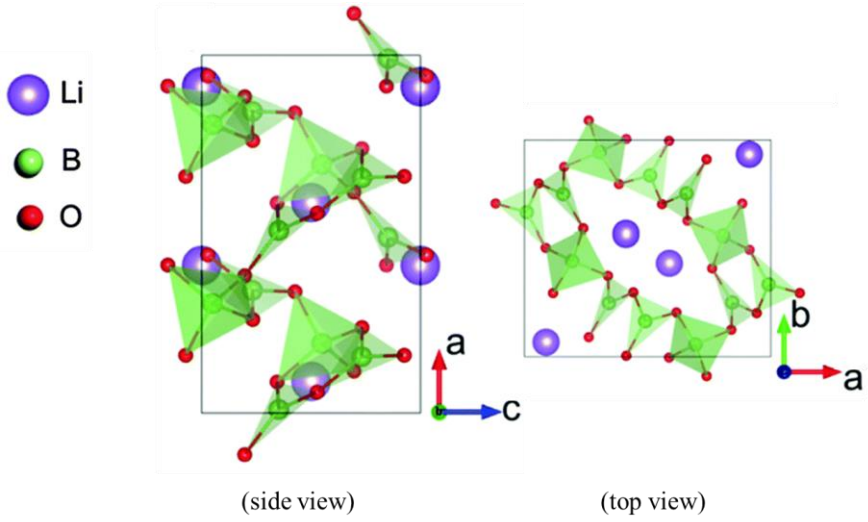

Fig. 4.4 Crystal structure of LiB_3O_5.[5)]

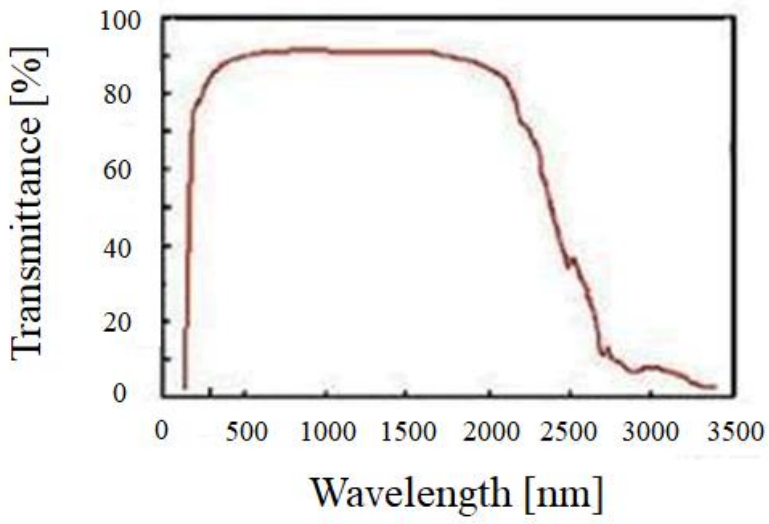

Fig. 4.5 Transmittance spectra of LiB_3O_5.[6)]

[2] $KTiOPO_4$ (KTP)

A potassium titanyl phosphate (KTP, see Fig. 4.6)[7-9)] is a nonlinear crystal with high nonlinearity, and it allows us to develop an efficient 2 μm OPO by type-II birefringence phase matching.

However, its large birefringence induces significant walk-off effect, in which the light wave with an extraordinary polarization propagates towards a different direction from the

Poynting vector (energy flow direction) as shown in Fig. 4.7. Such walk-off effect often impacts the nonlinear interaction length and degrades the beam quality of the signal and idler.

In order to compensate such walk-off effect, cascaded KTP crystals[10] with inverted orientations are used in this work (see Fig. 6.1).

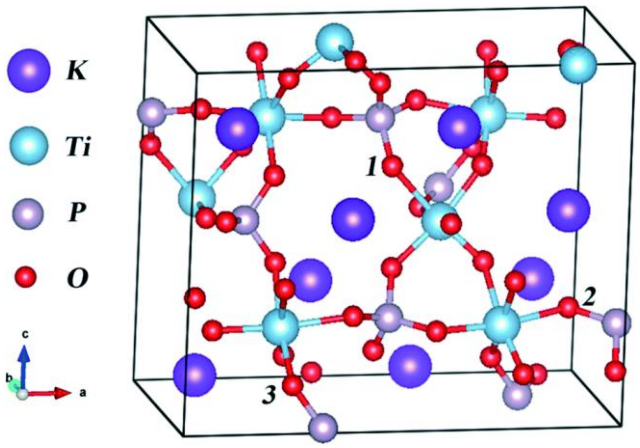

Fig. 4.6 Crystal structure of $KTiOPO_4$.[11]

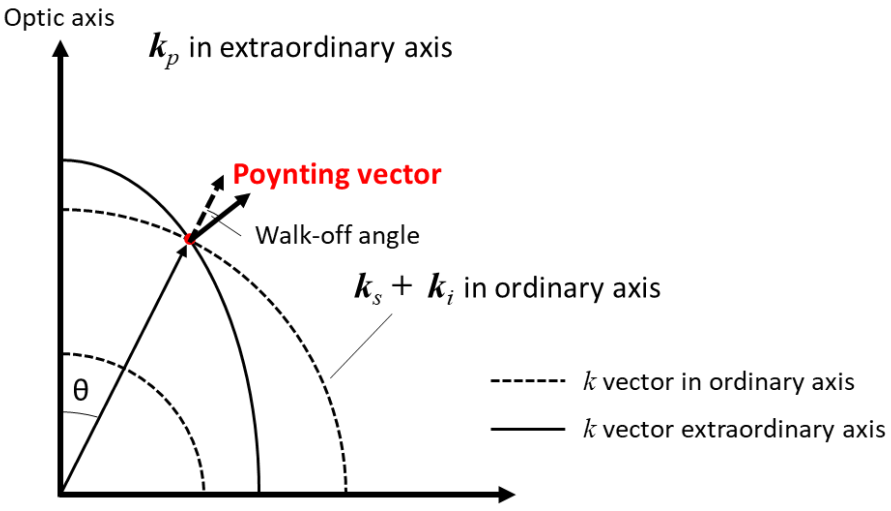

Fig. 4.7 Walk-off effect.

[3] $AgGaSe_2$ (AGS)

$AgGaSe_2$ crystal possesses a high transparency (see Fig. 4.8, transmittance spectra measured by Fourier-transform infrared spectroscopy) and a large nonlinearity in mid-infrared region, which allows to produce the mid-infrared output by optical parametric oscillation or difference frequency generation.

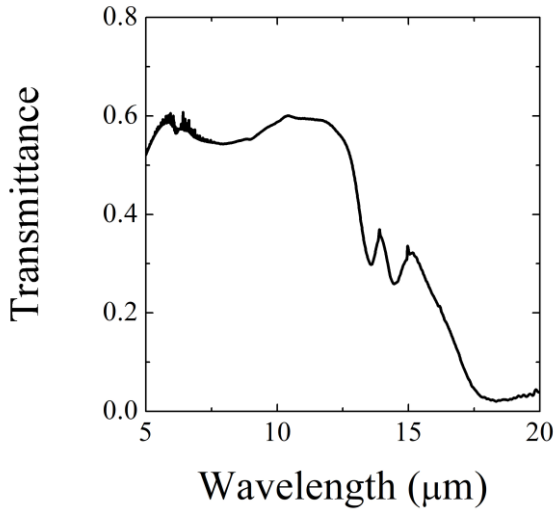

Fig. 4.8 Transmittance spectra of $AgGaSe_2$ crystal measured by Fourier-transform infrared spectroscopy.

4.3 Coupled-wave equations

In this section, the coupled-wave equations to analyze the three waves (the pump, signal and idler) interaction are presented.

The nonlinear traveling equation including the second order nonlinear polarization can be obtained as follows:

$$\nabla^2 \boldsymbol{E} - \mu \frac{\partial^2}{\partial t^2}(\varepsilon_0 \boldsymbol{E} + \boldsymbol{P}^{(1)}) = \mu \frac{\partial^2 \boldsymbol{P}^{(2)}}{\partial t^2}$$
$$\nabla^2 \boldsymbol{E} - \mu\varepsilon \frac{\partial^2}{\partial t^2}\boldsymbol{E} = \mu \frac{\partial^2 \boldsymbol{P}^{(2)}}{\partial t^2}. \quad (4.5)$$

This equation represents the behavior of the electric fields, $\boldsymbol{E}$, originated from the second order nonlinear polarization $\boldsymbol{P}^{(2)}$. The $\boldsymbol{E}$ is the superposed state of three electric fields

(with a frequency of ω_1, ω_2, and ω_3, respectively) interacting in this process, as written by eq. (4.6).

$$E(z,t) = \sum_{m}^{3} E_m(z,t) = \sum_{m}^{3} E_m(z)\exp[i(\omega_m t - k_m z)] + c.c \tag{4.6}$$

The $\boldsymbol{P}^{(2)}$ is also the nonlinear polarization in a frequency of $\omega_1 = \omega_3 - \omega_2$, $\omega_2 = \omega_3 - \omega_1$, and $\omega_3 = \omega_1 + \omega_2$, given by eqs.(4.7)-(4.9).

$$P^{(2)}_{\omega_3-\omega_2}(z,t) = \varepsilon_0 \chi_{jk} a_{3j} a_{2k} E_3 E_2^* \exp[i(\omega_3 - \omega_2)t - (k_3 - k_2)z], \tag{4.7}$$

$$P^{(2)}_{\omega_3-\omega_1}(z,t) = \varepsilon_0 \chi_{jk} a_{3j} a_{1k} E_3 E_1^* \exp[i(\omega_3 - \omega_1)t - (k_3 - k_1)z], \tag{4.8}$$

$$P^{(2)}_{\omega_1+\omega_2}(z,t) = \varepsilon_0 \chi_{jk} a_{1j} a_{2k} E_1 E_2 \exp[i(\omega_1 + \omega_2)t - (k_1 + k_2)z], \tag{4.9}$$

where a is the unit vector of the polarization of the three electric fields, respectively. Substituting eqs. (4.7)-(4.9) for eq. (4.5) and utilizing the SVA approximation, the following equations can be obtained.

$$\frac{dE_1}{dz} = -\frac{i\omega_1}{2}\sqrt{\frac{\mu}{\varepsilon_1}}\, dE_3 E_2^* \tag{4.10}$$

$$\frac{dE_2^*}{dz} = +\frac{i\omega_2}{2}\sqrt{\frac{\mu}{\varepsilon_2}}\, dE_1 E_3^* \tag{4.11}$$

$$\frac{dE_3}{dz} = -\frac{i\omega_3}{2}\sqrt{\frac{\mu}{\varepsilon_3}}\, dE_1 E_2 \tag{4.12}$$

These equations are well-known as the coupled-wave equations among three waves, in which $d(=\varepsilon_0\chi_{jk})$ is the nonlinear coefficient for nonlinear materials, and $k_3 - k_2 = k_1$ is established.

4.4 Interaction in optical parametric process

Above mentioned coupled-wave equations explain the interaction among the pump, signal and idler.

The couple parameter κ_m is defined by eq. (4.13).

$$\kappa_m = \frac{\omega_m}{2} d \sqrt{\frac{\mu}{\varepsilon_m}} \tag{4.13}$$

The coupled wave equations can be then rewritten as follows:

$$\frac{dE_1}{dz} = -i\kappa_1 E_3 E_2^*, \tag{4.14}$$

$$\frac{dE_2^*}{dz} = +i\kappa_2 E_1 E_3^*. \tag{4.15}$$

Assuming that the pump power (ω_3) is much larger than the signal and idler (ω_1, ω_2) powers, namely the pump power is regarded as constant, eqs. (4.14) and (4.15) are simplified to be

$$\frac{dE_1}{dz} = -ig_1 E_2^*, \tag{4.16}$$

$$\frac{dE_2^*}{dz} = +ig_2^* E_1, \tag{4.17}$$

where g_m, is often referred to as couple constant.

$$g_m = \frac{\omega_m}{2} d \sqrt{\frac{\mu}{\varepsilon_m}} E_3(0) \tag{4.18}$$

Combining eqs. (4.16) and (4.17),

$$\frac{d^2 E_1}{dz^2} = g_1 g_2^* E_1 = \frac{1}{4} \frac{\omega_1 \omega_2}{n_1 n_2} \left(\frac{\mu}{\varepsilon_0}\right) d^2 |E_3(0)|^2. \tag{4.19}$$

Therefore, the solutions for eqs. (4.16) and (4.17) can be obtained as follows:

$$E_1(z) = E_1(0)\cosh(|g|z), \tag{4.20}$$

$$E_2^*(z) = i\frac{g}{|g|} E_1(0)\sinh(|g|z), \tag{4.21}$$

$$g = \frac{1}{2} \sqrt{\frac{\omega_1 \omega_2}{n_1 n_2} \left(\frac{\mu}{\varepsilon_0}\right)} dE_3(0). \tag{4.22}$$

The following relationship between the signal and idler (ω_1, ω_2) waves is established.

$$E_1(z) = E_1(0)\cosh(|g|z) - i\frac{g}{|g|}E_2^*(0)\sinh(|g|z) \tag{4.23}$$

$$E_2^*(z) = E_2^*(0)\cosh(|g|z) + i\frac{g}{|g|}E_1(0)\sinh(|g|z) \tag{4.24}$$

When $|g|z \gg 1$, both the signal and idler exponentially increase [so called optical parametric amplification (OPA)]. Also note that zero-point quantum fluctuations can act as a seed input, namely, injection of the signal or idler is not required.

4.5 Optical parametric oscillator (OPO)

The optical parametric cavity configuration, in which the nonlinear crystal is located, is required to yield sufficiently signal and idler outputs. The cavity is generally formed of a pair of mirrors with a high reflectivity for one or the other (or both) of the signal and idler (Fig. 4.9), so that the amplification is achieved by successive-passes.

When the gain overcomes the cavity loss via round-trip in the cavity, the signal or idler (or both) starts to lase, and it is extracted from the cavity. The cavity loss includes output coupling loss, transmission loss of the nonlinear crystal, and diffraction loss.

The parametric oscillation process is as follows. Once the parametric gain is equal to the cavity loss, the parametric cavity starts to oscillate. In steady state, the signal and idler powers are determined as an increment of the pump power by the parametric gain (, which is equal to the cavity loss).

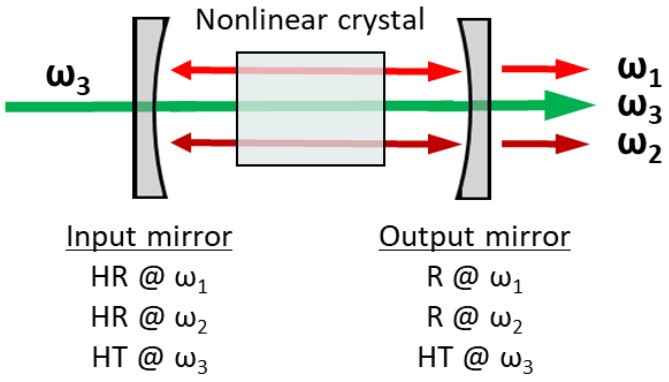

Fig. 4.9 Schematic diagram of an optical parametric oscillator.

4.6 Singly/Doubly-resonant oscillators

The OPO with a high Q cavity configuration for the signal or idler (so called singly resonant cavity configuration) is mostly employed [Figs. 4.10(a) and (b)]. In the singly-resonant cavity for the signal (ω_1), the electric field of the idler (ω_2) with propagation through the nonlinear crystal can be regarded as constant. The resulting amplitude of the idler grows linearly with propagation direction *z* as follows:

$$E_2^*(z) = +i\kappa_2 E_1 E_3^* z. \tag{4.25}$$

Substituting eq. (4.25) into eq. (4.14), the following formula is obtained.

$$\frac{\Delta E_1}{E_1} = \kappa_1 \kappa_2 E_3 E_3^* L^2, \tag{4.26}$$

where L is the crystal length. Further developing the above equation by utilizing the relation between the increase in electric field and in intensity, $dI_1/I_1 = 2 \cdot dE_1/E_1$, and the relation between the electric field and intensity, $I = n\sqrt{\varepsilon_0/\mu_0}|E|^2/2$,

$$\frac{\Delta I_1}{I_1} = \frac{\omega_1 \omega_2}{n_1 n_2 n_3}\left(\frac{\mu_0}{\varepsilon_0}\right)^{3/2} I_3(0) d^2 L^2. \tag{4.27}$$

This is the parametric gain per round-trip, being equal to the cavity loss, given by $\alpha_1 I_1$, in which α_1 represents the round-trip loss for the signal.
Hence, the incident pump intensity required for the parametric oscillation, $I_3(0)$, is given by

$$I_3(0) = \alpha_1 \Big/ \left(\frac{\omega_1 \omega_2}{n_1 n_2 n_3}\left(\frac{\mu_0}{\varepsilon_0}\right)^{3/2} d^2 L^2\right). \tag{4.28}$$

A doubly-resonant cavity configuration, in which both the signal and idler circulate in the cavity (Fig. 4.9), the signal and idler can be written as

$$\Delta E_1 = -i\kappa_1 E_3 E_2^* L, \tag{4.29}$$
$$\Delta E_2^* = +i\kappa_2 E_1 E_3^* L. \tag{4.30}$$

Assuming that the signal (idler) is amplified in phase with the already existing field, the below relation is established.

$$\Delta I_m = \sqrt{\frac{\varepsilon_m}{\mu_0}}|E_m||\Delta E_m| \tag{4.31}$$

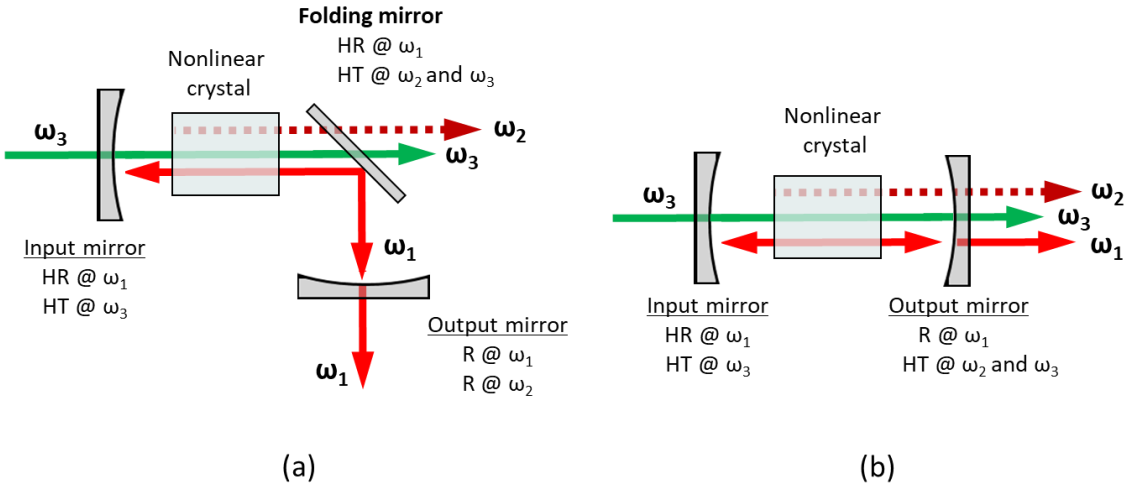

Fig. 4.10 Schematic diagrams of the singly-resonant (a) folding and (b) linear cavity configurations.

Thus, by substituting eqs. (4.29) and (4.30) for eq. (4.31), the parametric gain per round-trip is derived by

$$\Delta I_1 = \sqrt{\frac{\varepsilon_1}{\mu_0}} E_1 |\Delta E_1| = \sqrt{\frac{\varepsilon_1}{\mu_0}} |E_1||E_3||E_2^*| \kappa_1 L = \alpha_1 I_1, \tag{4.32}$$

$$\Delta I_2 = \sqrt{\frac{\varepsilon_2}{\mu_0}} E_2 |\Delta E_2| = \sqrt{\frac{\varepsilon_2}{\mu_0}} |E_2||E_1||E_3^*| \kappa_2 L = \alpha_2 I_2. \tag{4.33}$$

Taking the product of these equations, the relationship in terms of the oscillation threshold in the doubly-resonant cavity can be derived.

$$\frac{\omega_1 \omega_2}{n_1 n_2 n_3} \left(\frac{\mu_0}{\varepsilon_0}\right)^{3/2} d^2 L^2 I_3(0) = \frac{\alpha_1 \alpha_2}{2} \tag{4.34}$$

This formula indicates that the oscillation threshold in the doubly-resonant cavity is approximately a half of that of the singly-resonant cavity. In fact, it is possible to form the OPO based on the doubly-resonant cavity by continuous wave (CW) pumping, although it has a drawback in the wavelength-tuning of the signal and idler, e.g. the wavelengths jump.

4.7 Optical vortex pumped optical parametric oscillators

As above-mentioned, two conservation laws, i.e. photon energy and momentum (phase-matching condition), is always established in the optical parametric process. In optical vortex pumping case, the OAM, i.e. topological charge, must be further conserved (Fig. 4.11). How is the topological charge of the pump beam divided into signal and idler outputs? It can be controlled by the optical parametric cavity configuration and characteristics of the nonlinear crystal used for the optical parametric oscillator.

With a type-II KTP crystal [pump (ordinary wave) → signal (ordinary wave) + idler (extraordinary wave)], the walk-off effects arising from the birefringence of the crystal prevents the idler output from lasing in a vortex mode, so that the topological charge of the pump beam is transferred to the signal output with the same ordinary wave as the pump (Fig. 4.12).[12,13)]

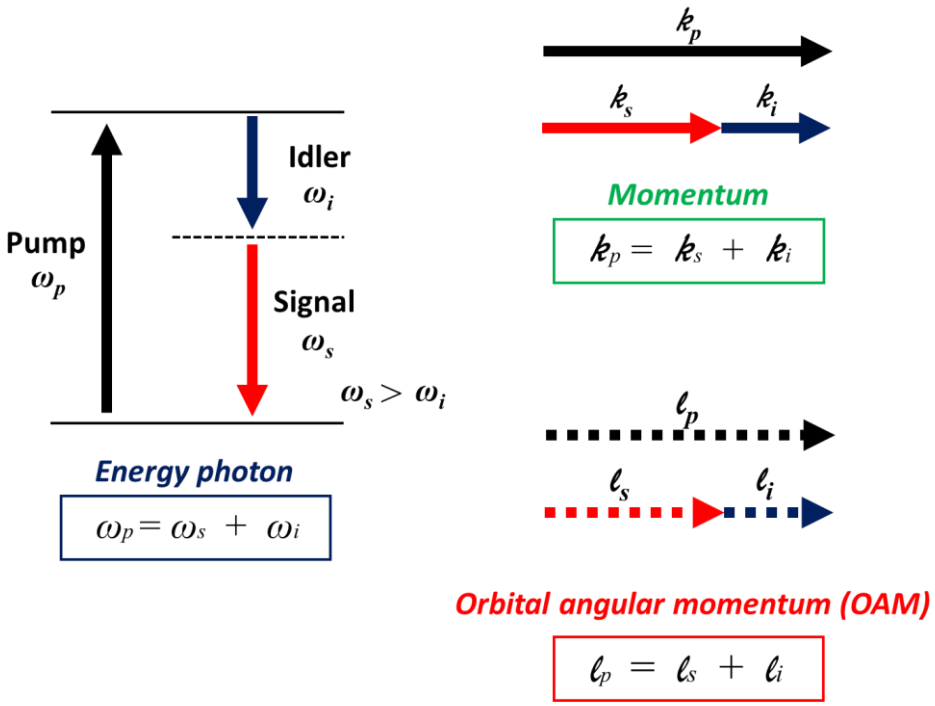

Fig. 4.11 Three conservation laws in the optical parametric process.

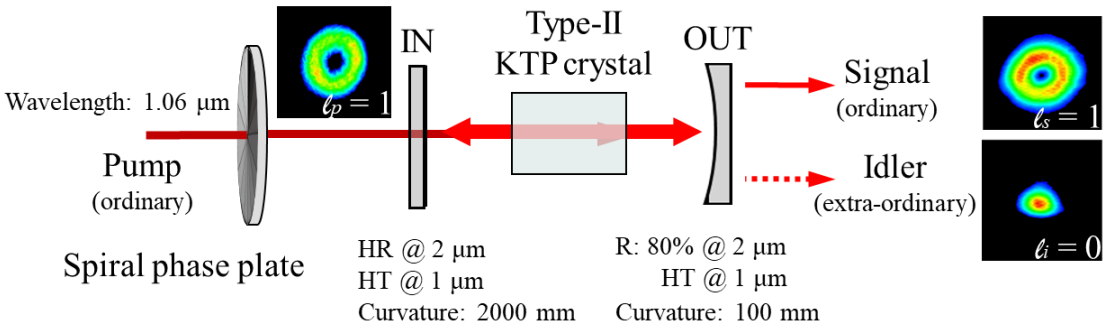

Fig. 4.12 Optical vortex pumped KTP optical parametric oscillator.

When a type-I LBO crystal [pump (extraordinary wave) → signal (ordinary wave) + idler (ordinary wave)] is used as the nonlinear crystal, the singly resonant parametric cavity must be formed, since both the signal and idler lase at a mix-mode (incoherent coupling between the Gaussian mode and the vortex mode) in the double resonant cavity.[14] If the cavity is singly resonant for the signal, the topological charge of the pump is selectively transferred to the signal (Fig. 4.13), on the other hand, if the singly resonant cavity for the idler, the idler lases at the vortex mode (Fig. 4.14).

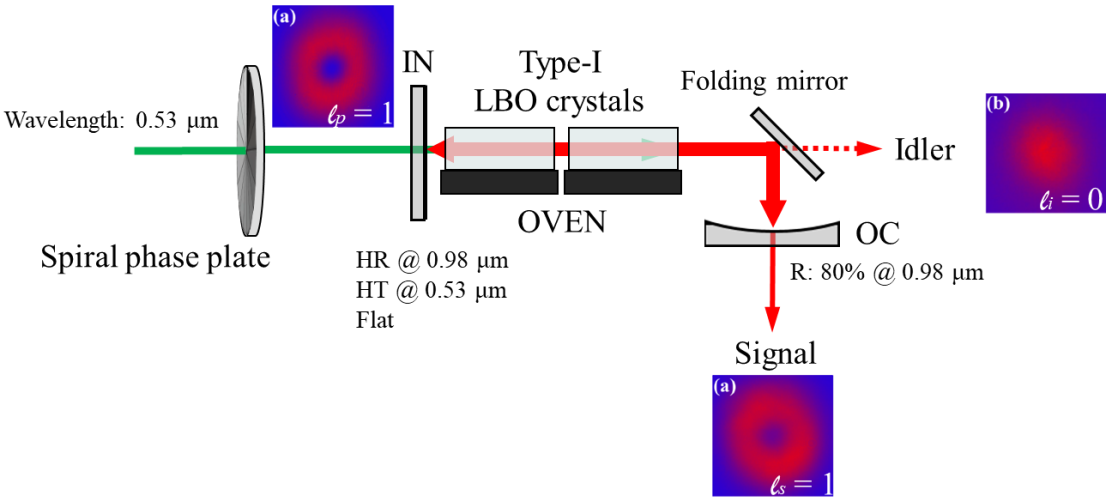

Fig. 4.13 LBO optical parametric oscillator with singly resonant cavity configuration for the signal output.

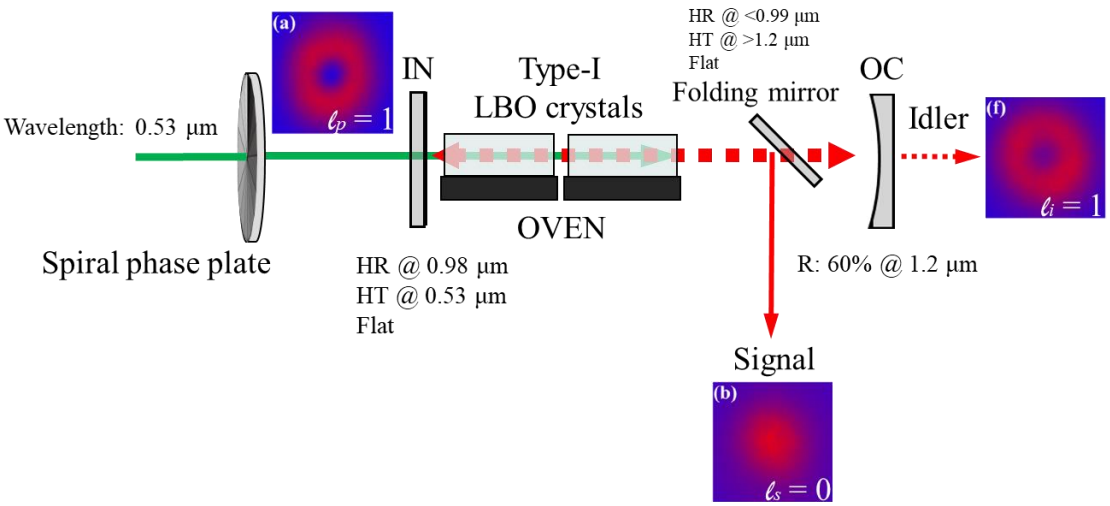

Fig. 4.14 LBO optical parametric oscillator with singly resonant cavity configuration for the idler output.

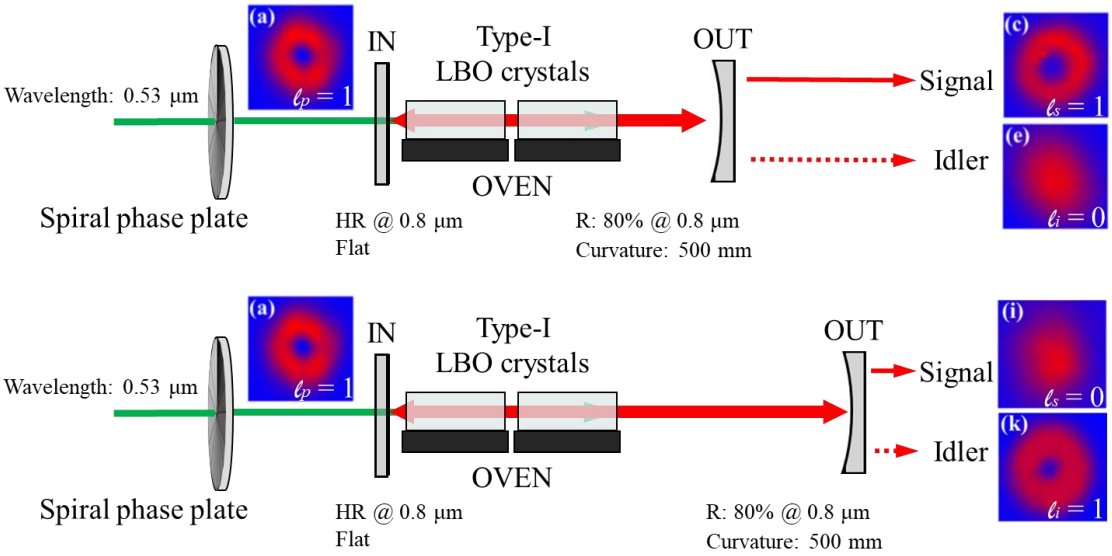

Fig. 4.15 Topological charge switching by tuning the cavity-length.

Topological charge switching in a linear cavity configuration with the singly resonance for the signal have been also realized by tuning the cavity-length (Fig. 4.15).[15] In this case, a compact cavity configuration forces the signal to lase in a vortex mode. With an

extended cavity configuration, the topological charges between the signal and idler are swapped, and conversely the idler carries the OAM as the vortex mode, while the signal exhibits the Gaussian mode. The mechanism was also addressed by Fresnel number (which is an indicator of cavity loss for the high-order mode).

4.8 References

1) N. M. Kroll, "Parametric amplification in spatially extended media and application to the design of tuneable oscillators at optical frequencies," Phys. Rev. **127**, 1207 (1962).
2) C. Chen, Y. Wu, A. Jiang, B. Wu, G. You, R. Li, and S. Lin, "New nonlinear-optical crystal: LiB_3O_5," J. Opt. Soc. Am. B **6**, 616 (1989).
3) S. Lin, Z. Sun, B. Wu, and C. Chen, "The nonlinear optical characteristics of a LiB_3O_5 crystal," J. Appl. Phys. **67**, 634 (1990).
4) D. N. Nikogosyan, "Lithium triborate (LBO)," Appl. Phys. A **58**, 181 (1994).
5) J. Li, Z. Ma, C. He, Q Li, and K. Wu, "An effective strategy to achieve deeper coherent light for LiB_3O_5," J. Mater. Chem. C. **4**, 1926 (2016).
6) http://www.castech-us.com/caslbo.htm
7) F. C. Zumsteg, J. D. Bierlein, and T. E. Gier, "$K_xRb_{1-x}TiOPO_4$: A new nonlinear optical material," J. Appl. Phys. **47**, 4980 (1976).
8) S. Dezhong and H. Chaoen, "A new nonlinear optical crystal KTP," Prog. Cryst. Growth Charact. **11**, 269 (1985).
9) L. K. Cheng and J. D. Bierlein, "KTP and isomorphs – recent progress in device and material development," Ferroelectrics **142**, 209 (1993).
10) D. J. Armstrong, W. J. Alford, T. D. Raymond, A. V. Smith, and M. S. Bowers, "Parametric oscillation with walkoff-compensating crystals," J. Opt. Soc. Am. B **14**, 460 (1997).
11) Y. Zhang, Y. Leng, J. Liu, N. Ji, X. Duan, J. Li, X. Zhao, J. Wang, and H. Jiang, "Mechanism of hydrogen treatment in $KTiOPO_4$ crystals at high temperature : experimental and first-principles," CrystEngComm. **17**, 3793 (2015).
12) T. Yusufu, Y. Tokizane, M. Yamada, K. Miyamoto, and T. Omatsu, "Tunable 2-μm optical vortex parametric oscillator," Opt. Express **20**, 23666 (2012).
13) T. Yusufu, Y. Tokizane, K. Miyamoto, and T. Omatsu, "Handedness control in a 2-μm optical vortex parametric oscillator," Opt. Express **21**, 23604 (2013).
14) A. Abulikemu, T. Yusufu, R. Mamuti, K. Miyamoto and T. Omatsu, "Widely-tunable vortex output from a singly resonant optical parametric oscillator**,**" Opt. Express **23**,

18338 (2015).
15) A. Abulikemu, T. Yusufu, R. Mamuti, S. Araki, K. Miyamoto and T. Omatsu, “Octave-band tunable optical vortex parametric oscillator,” Opt. Express **24**, 15204 (2016).

Chapter 5 – Ultra-broadband tunable (0.67-2.57 μm) optical vortex parametric oscillator

Wavelength–tunable optical vortex sources with versatile topological charge are required for the laser application, such as processing, fluorescence microscope, and spectroscopy, because it enables us to adjust the vortex wavelength to individual absorption bands (resonant frequencies) of materials. In this chapter, I present the tunable vortex source with ultra-broadband tunability (0.67-2.57 μm) based on optical parametric oscillator. This system also enables the topological charge switching in the range of -1 to 2.

5.1 Experimental setup

Figure 5.1 shows a schematic diagram of the optical vortex parametric laser with ultra-broadband wavelength-tunability. A frequency-doubled, diode-pumped Q-switched Nd:YAG laser (wavelength, 0.53 μm; pulse width, ~10 ns; pulse repetition frequency, 100 Hz; beam quality, M^2 ~1.1) is used as a pump source, and its output with a Gaussian transverse mode is converted to a 1st-order vortex mode with a topological charge of $\ell = 1$ via a spiral phase plate. The collimated annular pump beam with a beam radius of ~0.3 mm is carried to cascaded non-critical phase-matching LiB_3O_5 (NCPM-LBO) crystals ($3\times3\times45$ mm^3, $\theta = 90°$, $\varphi = 0°$, anti-reflection coating for 0.53 and 1.06 μm) mounted on an oven. Wavelength-tuning of the resulting signal and idler outputs is achieved by controlling the crystal-temperatures. This configuration including the pumping source with short pulse width of ~10 ns (i.e. with high peak power) and cascaded LBO crystals with 45 mm long each, provides high parametric gain, so that the further frequency tunability and power scalability of the vortex laser system can be expected.

The optical parametric cavity (0.8 μm high-Q cavity) is formed of a flat input mirror (IN) with high-reflectivity in the wavelength of 0.65-1.05 μm and a concave (curvature radius, 500 mm) output mirror (OUT) with 80% reflectivity at 0.8 μm, which acts as a singly resonant cavity for the signal output (the higher frequency output). The cavity with a high Q-factor at 0.7 μm (0.7 μm high-Q cavity) is also employed to cover the resulting frequency-gaps, where the optical vortex is not available, addressed in the section of experimental results. Figure 5.2 also shows the reflectance property of the output/input mirror used for the parametric cavity.

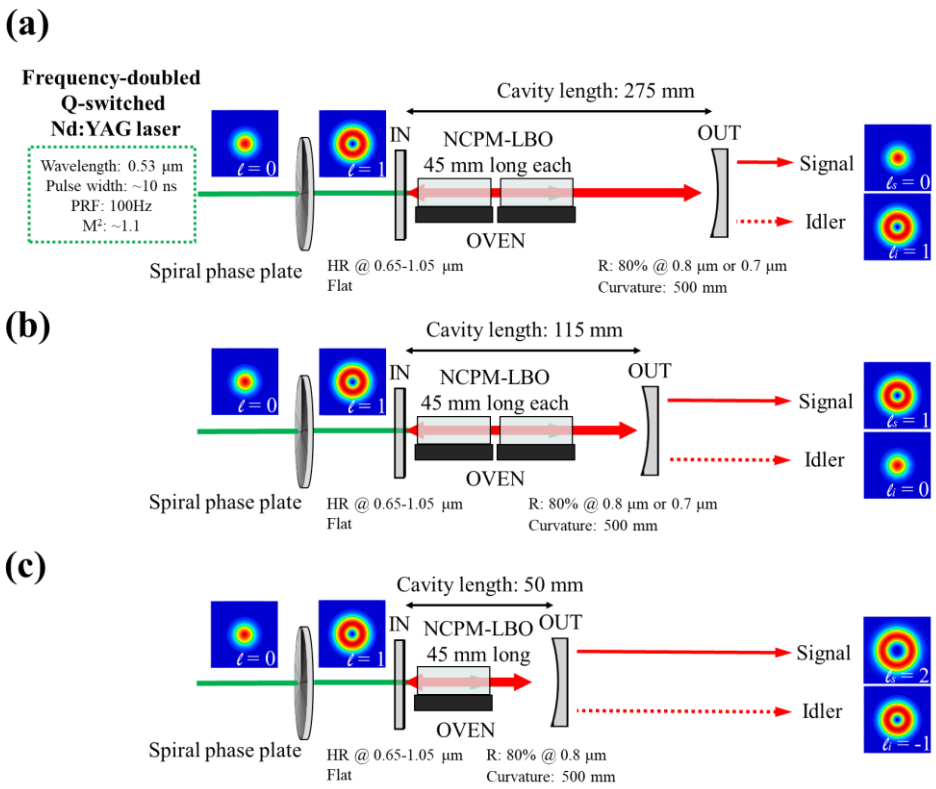

Fig. 5.1 Experimental setup for the ultra-broadband tunable optical vortex parametric laser with a versatility of a topological charge [optical vortex generation with a topological charge of (a) $\ell_s = 0$ and $\ell_i = 1$, (b) $\ell_s = 1$ and $\ell_i = 0$, (c) $\ell_s = 2$ and $\ell_i = -1$].

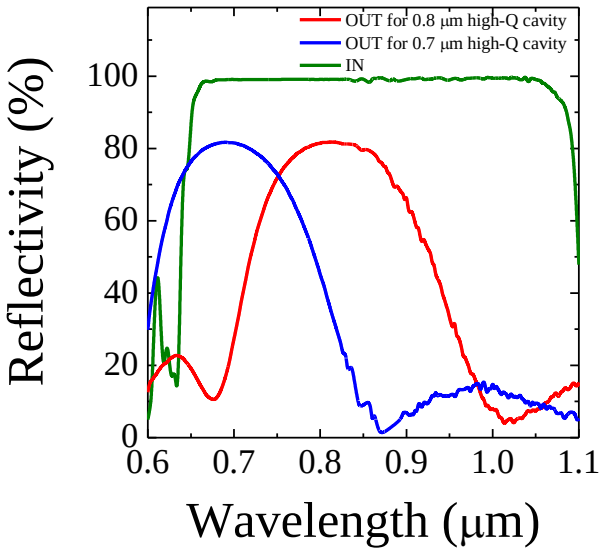

Fig. 5.2 Reflectance properties of input and output mirrors used.

In a singly resonant (for the signal) cavity configuration, the parametric gain for the signal with a topological charge of ℓ_s can be described by the spatial overlapping efficiency, η_{ℓ_s}, of electric field amplitudes between the pump and the signal in nonlinear crystal,[1,2] given by

$$\begin{aligned}\eta_{\ell_s} &= \int_0^\infty E_{pump}\, E_{signal}^{*} \cdot 2\pi r\, dr \\ &\propto \int_0^\infty r \exp\left(-\frac{r^2}{\omega_p^2}\right) \cdot r^{|\ell_s|} \exp\left(-\frac{r^2}{\omega_s^2}\right) \cdot 2\pi r\, dr,\end{aligned} \tag{5.1}$$

in which E_{pump} and E_{signal} are the normalized electric field amplitudes of the pump and the signal, respectively, ω_p (~0.3 mm) is the pump radius, and ω_s is the mode field size of the signal at various cavity lengths calculated by using the LASCAD software.

Figure. 5.3 shows the relative spatial overlapping efficiency estimated, g (η_1/η_0 and η_2/η_0), as a function of the cavity length, indicating the spatial mode the parametric gain dominantly acts on. When the cavity length is more than 210 mm, η_1/η_0 is less than 1 (i.e. η_0 is larger than η_1), thereby the parametric cavity will force the signal to lase at the fundamental Gaussian mode with a topological charge of ℓ_s = 0. The idler output is then expected to exhibit a 1st-order vortex mode with ℓ_i = 1, so as to conserve the topological charge of the pump beam [Fig. 5.1(a), defined as the extended cavity].

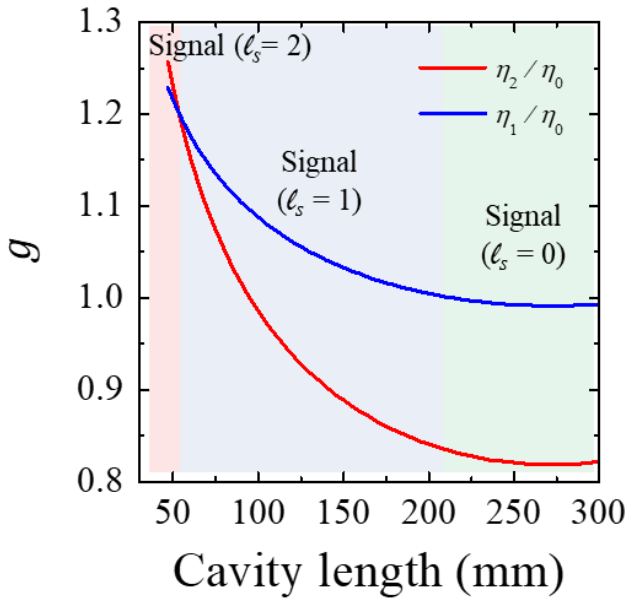

Fig. 5.3 Relative spatial overlapping efficiency at various cavity lengths. Red and blue lines represent η_2/η_0 and η_1/η_0, respectively.

With shortening the cavity length (in the range of 55~210 mm), the signal and idler outputs will carry a 1st-order optical vortex (ℓ_s = 1) and Gaussian (ℓ_i = 0), respectively [Fig. 5.1(b), defined as the compact cavity], as η_1 exceeds η_0 and η_2. When the cavity length is shortened as much as possible (~50 mm), the optical parametric oscillator will be also expected to yield the 2nd-order vortex (ℓ_s = 2) signal and -1st-order vortex (ℓ_i = -1) idler outputs [Fig. 5.1(c), defined as the further compact cavity]. In this case, note that a NCPM-LBO crystal is removed to shorten the cavity length.

The spatial forms and wavefronts of the signal and idler outputs emitted from the parametric cavity are also observed by a Si (or InGaAs) CCD camera in combination with a laterally self-referenced interferometer using a transmission grating with 10 lines/mm (Fig. 5.4).

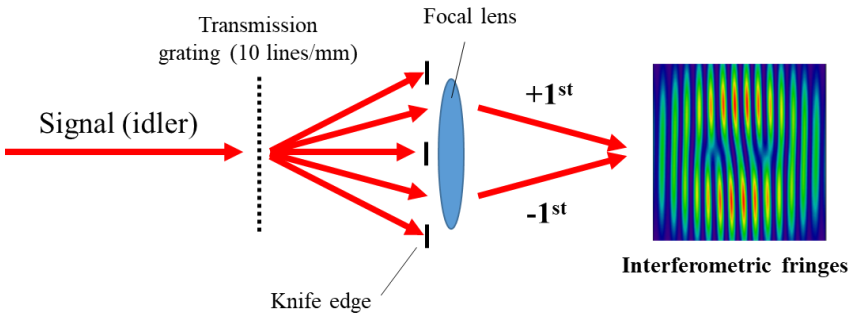

Fig. 5.4 Self-referenced interferometric technique using a transmission grating.

5.2 Experimental results

The spatial profiles and wavefronts for the pump beam, and the signal and idler outputs produced from the extended/compact parametric cavity are summarized in Fig. 5.5. The pump exhibited annular spatial mode and a pair of downward and upward Y-formed interferometric fringes [Figs. 5.5(a) and (b)], indicating a 1st-order vortex mode with a topological charge of ℓ = 1 (Appendix A.1). The extended cavity with a length of ~275 mm produced a Gaussian mode without any singularities as the signal output [Figs. 5.5(c) and (d)], and a 1st-order vortex mode with a topological charge of ℓ_i = 1 as the idler, as evidenced by the same interferometric fringes as the pump [Figs. 5.5(e) and (f)].

In contrast, the compact cavity with a length of ~115 mm allowed the signal to lase in a 1st-order optical vortex with ℓ_s = 1 [Figs. 5.5(g) and (h)], and then the idler output had a Gaussian mode with ℓ_i = 0 [Figs. 5.5(i) and (j)]. The beam quality factor, M^2 (see

Appendix A.2), of the vortex signal (idler) output was 2.03 (2.22), which gave close agreement with an ideal value, 2, of the 1st-order Laguerre-Gaussian mode, i.e. $LG_{0,1}$ mode (Fig. 5.6).[3)]

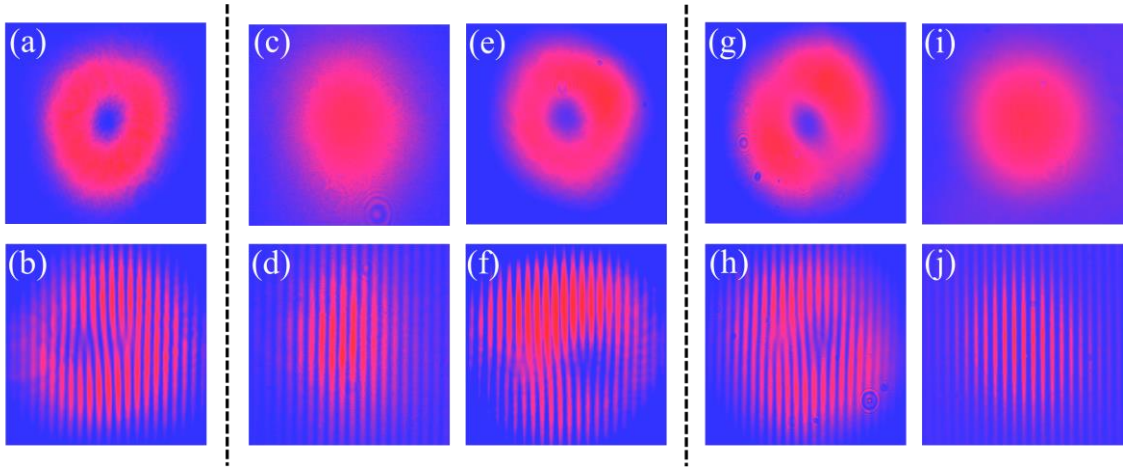

Fig. 5.5 (a) Spatial form and (b) interferometric pattern for the pump (0.53 μm). (c, e) Spatial forms and (d, f) interferometric patterns for the signal (0.93 μm) and idler (1.24 μm) produced from the extended cavity with a length of ~275 mm, respectively. (g, i) Spatial forms and (h, j) interferometric patterns for the signal (0.93 μm) and idler (1.24 μm) produced from the compact cavity with a length of ~115 mm, respectively.

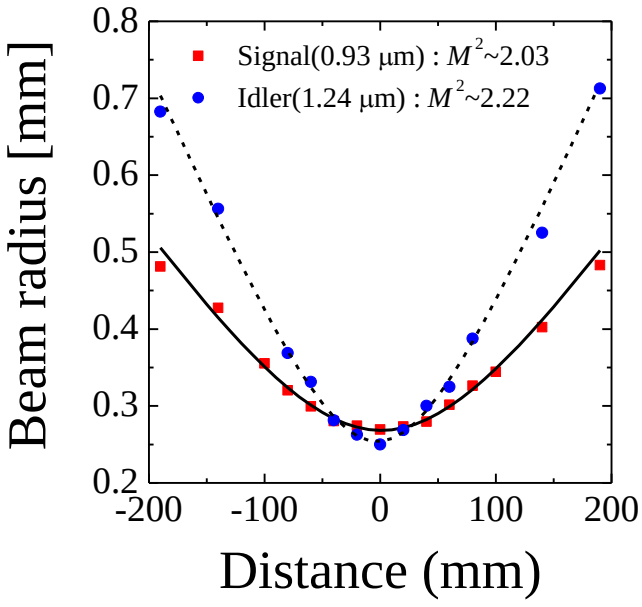

Fig. 5.6 Beam propagations of the vortex signal (0.93 μm) and idler (1.24 μm).

Figures 5.7 and 5.8 show the tunabilities of the optical vortex laser with the extended and compact cavity, respectively. In the extended cavity configuration, the vortex idler could be tuned in the wavelength range of 1.10–2.53 μm at pumping energy of 9 mJ. The signal output with a Gaussian mode was then obtained within 0.67-1.03 μm. The maximum vortex output energy was 1.6 mJ at a wavelength of 1.24 μm. With the compact cavity, the optical vortex as the signal output was generated in the wavelength region of 0.67-1.03 μm, while the Gaussian idler was produced in the region of 1.10-2.66 μm. The measured maximum energy was also 2.9 mJ at 0.93 μm. Thus, the optical vortex output was tunable over an extremely wide wavelength range of 0.67–2.53 μm (over 2-octave band), as shown in Fig. 5.9 (shows the tunabilities in terms of vortex outputs). However, there were three frequency gaps, where the vortex output was unavailable, in the wavelength regions of 0.68–0.73, 1.03–1.10, and 1.94–2.47 μm. Two frequency gaps (0.68–0.73 and 1.94–2.47 μm) was originated from two wavelength-combinations of phase matching between the signal and idler outputs. Note that another frequency gap (1.03–1.10 μm) occurred owing to a double resonance for the signal and the idler.

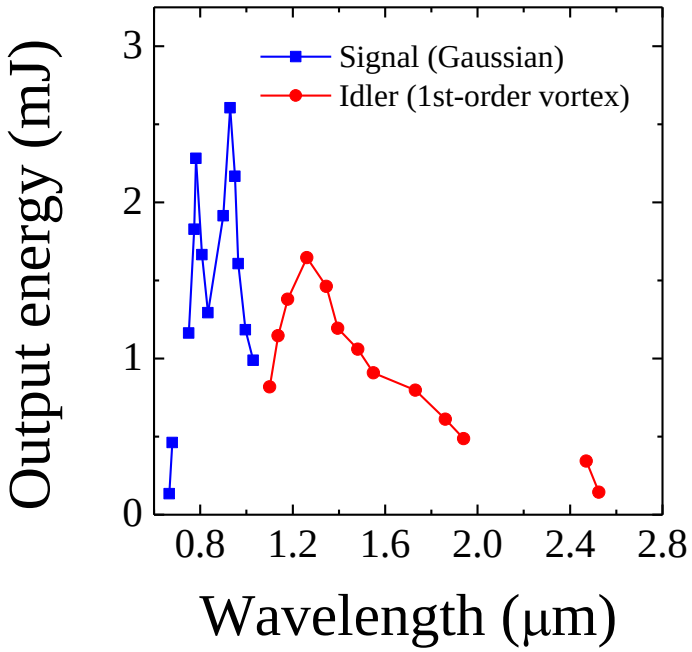

Fig. 5.7 Tunabilities of the optical vortex parametric laser with the extended cavity configuration. Blue square and red circle show the signal and idler outputs, respectively.

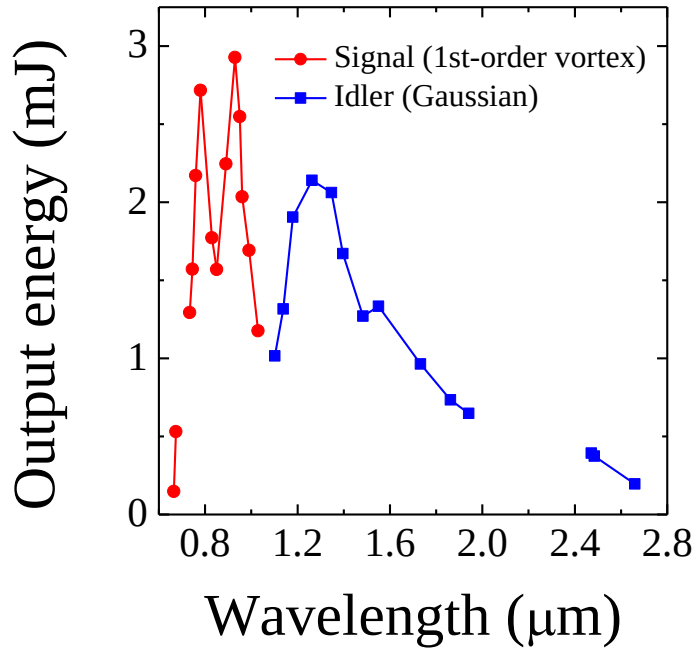

Fig. 5.8 Tunabilities of the optical vortex parametric laser with the compact cavity configuration. Red circle and blue square show the signal and idler outputs, respectively.

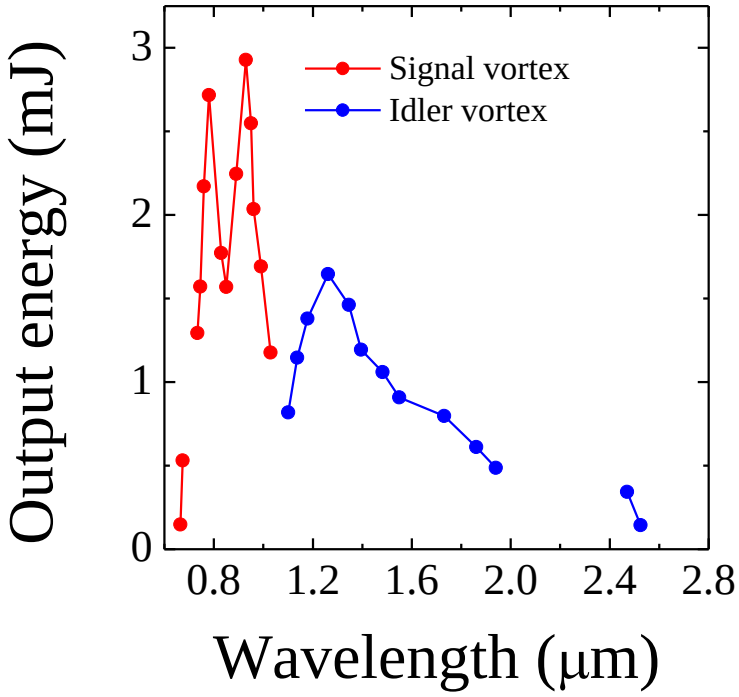

Fig. 5.9 Tunabilities of the optical vortex output with a topological charge of $\ell = 1$.

The theoretical tuning curve (the relationship between the resulting signal/idler wavelength and the LBO crystal temperature), calculated by utilizing the wavelength-dispersion equation and the Sellmeier equation for the crystal[4], are shown in Fig. 5.10. The temperature range of 109–157 ºC establishes two wavelength-combinations between the signal (0.68–0.73 or 0.73–1.03 μm) and idler (2.47-1.94 or 1.94–1.10 μm) as the non-critical phase matching condition. The 0.8 μm high-Q cavity (i.e. resonant cavity for 0.8 μm) stimulates the lasing of the signal in the wavelength range of 0.73–1.03 μm, thereby preventing generation in the wavelength range of 2.47-1.94 μm for the idler. As a result, two frequency gaps arose in the wavelength ranges of 0.68–0.73 and 2.47–1.94 μm.

Such frequency gaps were covered by employing the 0.7 μm high-Q cavity, in which the output mirror with ~80 % reflectivity (Fig. 5.2) in the wavelength range of 0.68-0.73 μm was utilized. With this system, the vortex signal (idler) output could be generated within 0.66 to 0.75 μm (2.57 to 1.93 μm) by varying a temperature in a range of 109 to 200 ºC. Therefore, the tunability of this optical vortex parametric laser system was 0.66–2.57 μm except a small frequency gap around the degenerate-wavelengths (1.03–1.10 μm), as shown in Fig. 5.11. I note the maximum wavelength of the idler was restricted by the transparency for the LBO (0.15–2.6 μm).[5]

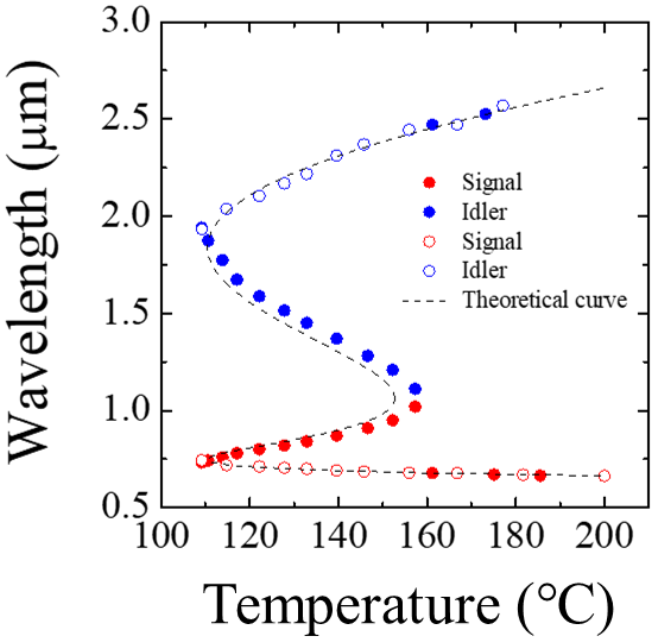

Fig. 5.10 Wavelengths of the signal (red) and idler (blue) outputs against the LBO crystal-temperature. The broken line represents the theoretical tuning curve of the optical parametric oscillation. The filled/open circles show the signal and idler emitted from a 0.8 μm/0.7 μm high-Q cavity.

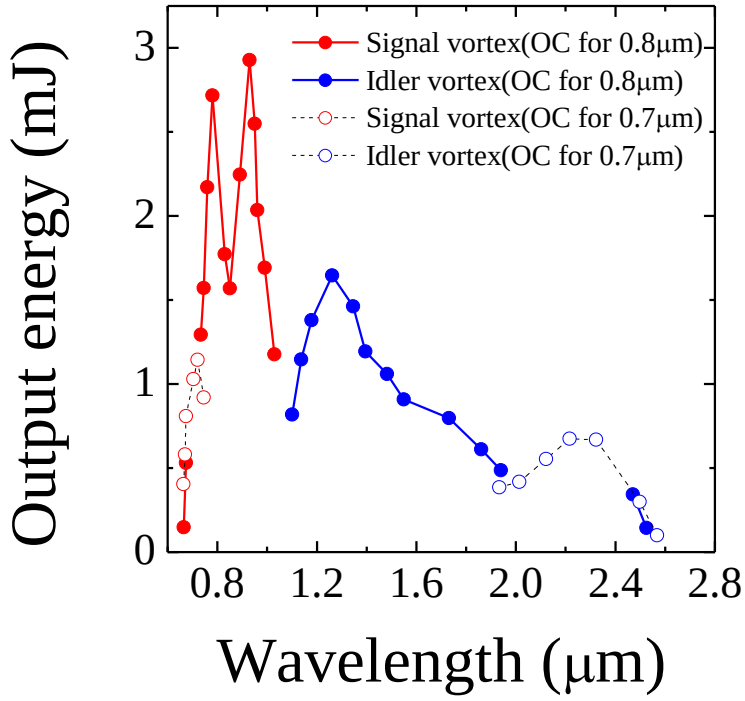

Fig. 5.11 Tunabilities of the optical vortex parametric laser. The filled and open circles are the vortex outputs produced from the parametric cavity with high-Q for 0.8 and 0.7 μm, respectively.

Curiously, a further compact cavity with a length of ~50 mm also enabled the production of the 2nd-order vortex signal (with ℓ_s = 2) and -1st-order vortex idler (with ℓ_i = -1), as evidenced by a pair of downward and upward fork fringes with 3 branches, and a pair of upward and downward fork fringes with 2 branches, respectively [Figs. 5.12(a)-(d)]. The 2nd-order and -1st-order vortex mode could be generated in the wavelength range of 0.76-0.97 μm and 1.19-1.78 μm, respectively, as shown in Fig. 5.13. Such an optical vortex generation with up-converted topological charge (i.e. a higher topological charge than that of pump beam) is first demonstration in the optical vortex pumped optical parametric oscillator.

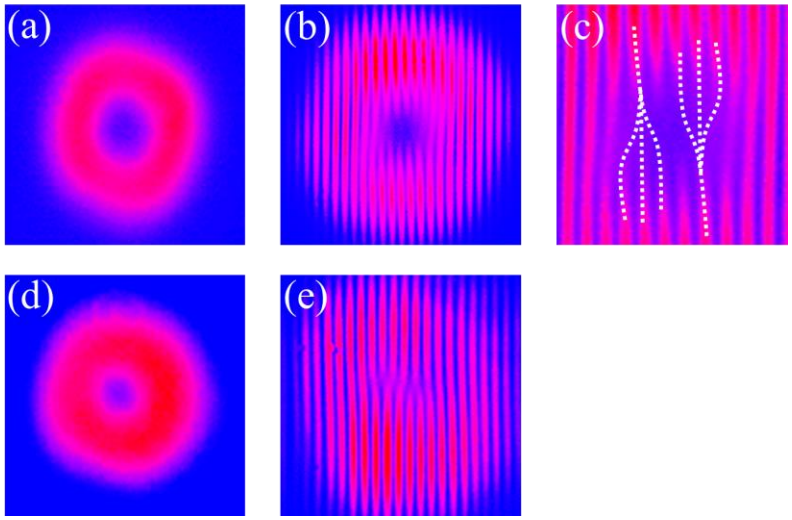

Fig. 5.12 (a) Spatial form, (b) interferometric pattern and (c) expanded view of the interferometric pattern of the signal output (0.93 μm) generated from a further compact cavity, respectively. (d) Spatial form and (e) interferometric pattern for the idler output (1.24 μm) generated from a further compact cavity, respectively.

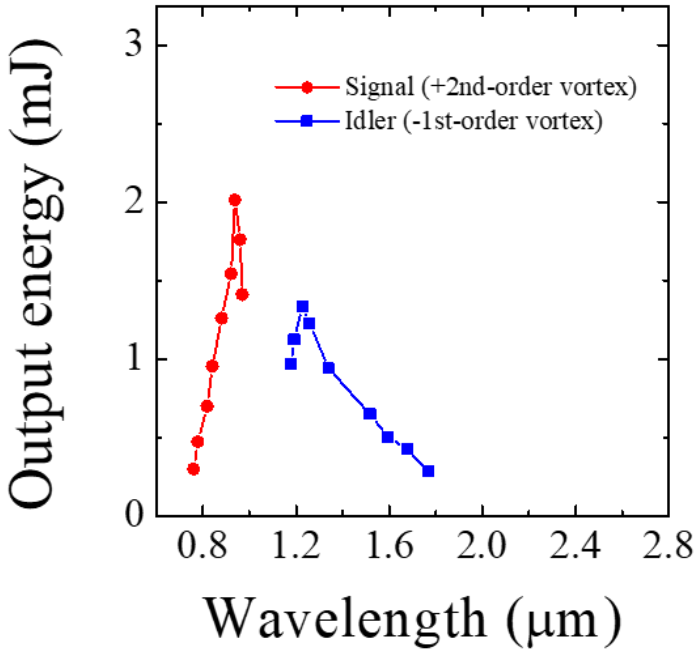

Fig. 5.13 Tunabilities of the optical vortex parametric laser with the further compact cavity configuration (cavity length of ~50 mm).

5.3 Discussion

The frequency gap around the degenerate-wavelengths (1.03–1.10 μm) resulted from a doubly resonant condition, i.e. resonance for both the signal and idler outputs, is focused on. Within the region, the signal and idler were forced to lase at a radial opening spatial mode [Figs. 5.14(c) and (f)], arising from coherent superposition between the vortex (ℓ = 1) and Gaussian (ℓ = 0) modes.[6,7] It indicates the signal and idler outputs possessed a non-integer topological charge, generally termed as a "fractional vortex mode". Why did the optical parametric oscillator with a stable cavity configuration yield such fractional vortex modes?

As shown in Fig. 5.15, the pumping source used in this work emitted Q-switched pulses with little modulation, meaning it lased in a few longitudinal modes. In fact, the spectral linewidth was estimated to be approximately 90 MHz based on the coherence length of ~3.3 m (defined as width at half-maximum of the exponential function fitted for the experimental plots), derived from the temporal coherence function obtained by the Michelson interferometer (Fig. 5.16) (see Appendix A.3). A beating (with a period of ~1.1 ns) of the coherence function also corresponds to the cavity length (~33 cm) of the pumping source. Such a pump source with narrow bandwidth induced the coherent-coupling between the Gaussian and vortex modes.

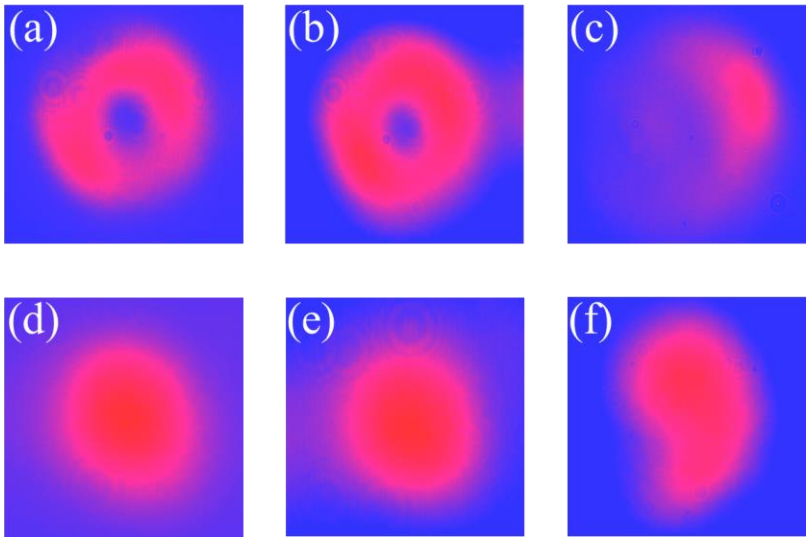

Fig. 5.14 Spatial forms of the signal output produced from the compact cavity at a wavelength of (a) 1.02 μm, (b) 1.03 μm, and (c) 1.04 μm, respectively. Spatial forms of the idler output produced from the compact cavity at a wavelength of (d) 1.11 μm, (e) 1.10 μm, and (f) 1.09 μm, respectively.

Also, the relatively short pulse with of ~10 ns causes only a few round-trips in the parametric cavity for the resonant mode, thus resulting in the coherent-coupling between the two modes owing to a small Gouy phase mode dispersion.

Further filling in the frequency gap originating from the double resonance condition will be achieved by employing an output/input mirror with much higher loss for the idler output in the degenerate-wavelengths region, so as to suppress a doubly resonance.

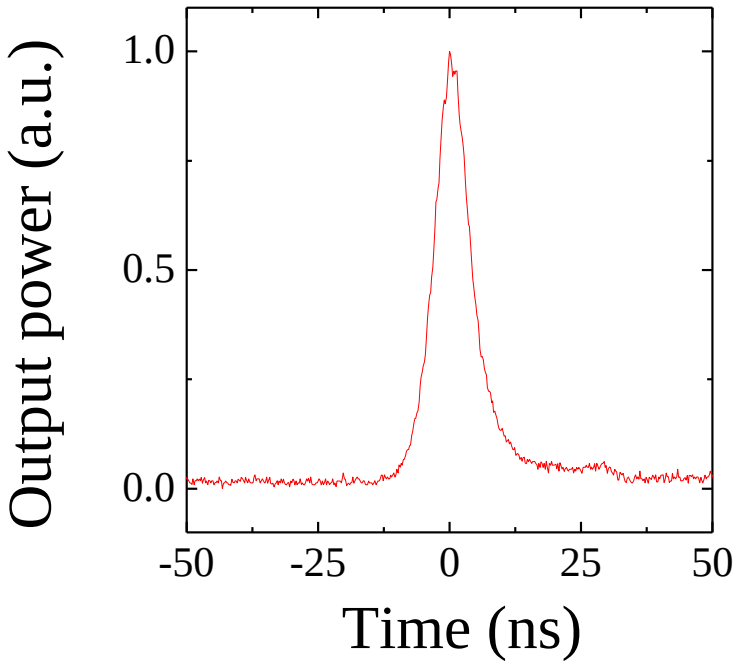

Fig. 5.15 Temporal waveform of the pumping source.

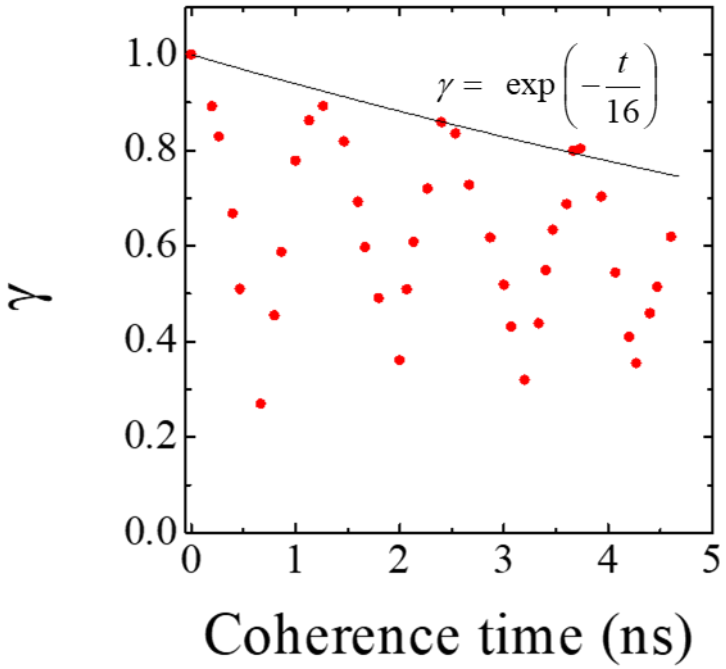

Fig. 5.16 Temporal coherence function of the pumping source.

5.4 Conclusion

An optical vortex source with ultra-broadband wavelength-tunability has been demonstrated by utilizing a LiB_3O_5 optical parametric oscillator (OPO) pumped by the optical vortex pulse with a short pulse duration (~10 ns). The system enabled us to generate the optical vortices with a pulse energy of >0.1 mJ (Maximum output energy, 2.9 mJ) in a wavelength range of 0.67–2.57 μm (over a 2-octave band with little frequency gap). The availability of the topological charge also ranged from -1 to 2.

Higher-order optical vortex generation will be possible by use of a higher-order optical vortex pumping. An ultra-broadband tunable optical vortex generation system without exchanging of the output mirror can be achieved by arrangement of the wavelength-selective elements, e.g. birefringence filter, in the parametric cavity

5.5 References

1) S. J. Brosnan, R. L. Byer, “Optical parametric oscillator threshold and linewidth studies,” IEEE J. Quantum Electron. **15**, 415 (1979).
2) A. Aadhi, G. K. Samanta, S. Chaitanya Kumar, and M. Ebrahim-Zadeh, “Controlled switching of orbital angular momentum in an optical parametric oscillator,” Optica **4**, 349 (2017).
3) S. Saghafi, C. J. R. Sheppard, “The beam propagation factor for higher order Gaussian beams,” Opt. commun. **153**, 207 (1998).
4) K. Kato, “Temperature-tuned 90/spl deg/phase-matching properties of LiB/sub 3/O/sub 5,” IEEE J. Quantum Electron. **30**, 2950 (1994).
5) C. Chen, Y. Wu, A. Jiang, B. Wu, G. You, R. Li, and S. Lin, “New nonlinear-optical crystal: LiB_3O_5,” J. Opt. Soc. Am. B **6**, 616 (1989).
6) W. M. Lee, X.-C. Yuan, and K. Dholakia, “Experimental observation of optical vortex evolution in a Gaussian beam with an embedded fractional phase step,” Opt. Commun. **239**, 129 (2004).
7) S. H. Tao, X-C. Yuan, J. Lin, X. Peng, and H. B. Niu, “Fractional optical vortex beam induced rotation of particles,” Opt. Express **13**, 7726 (2005).

Chapter 6 – Ultra-widely tunable mid-infrared (6-18 μm) optical vortex source

In this chapter, the further extension of the vortex lasing wavelength based on a difference frequency generator pumped by an optical vortex parametric oscillator is presented. This system enables the production of the optical vortices in the mid-infrared region (6-18 μm) and the handedness (sign of the topological charge) control of the vortex beam.

6.1 Difference frequency generation using optical vortex

As mentioned in section 4.3, the coupled-wave equations for the DFG ($\omega_s > \omega_i$) process without including absorption can be expressed as follows:

$$\frac{dE_D}{dz} = -\frac{i\omega_D}{2}\sqrt{\frac{\mu}{\varepsilon_D}}\,dE_s E_i^* \exp[-i(\Delta k)z], \tag{6.1}$$

where E_D, E_s, and E_i are the electric fields of the difference frequency, signal, and idler outputs, respectively. When conversion efficiency is low, the energy depletion of the signal and idler is negligible. Thus, by integrating in the range of z = 0~L (nonlinear crystal length, L), $E_D(L)$ is obtained as follows:

$$\begin{aligned} E_D(L) &= -\frac{i\omega_D}{2}\sqrt{\frac{\mu}{\varepsilon_D}}\,dE_s E_i^* \int_0^L \exp[-i(\Delta k)z]\,dz \\ &= -\frac{i\omega_D}{2}\sqrt{\frac{\mu}{\varepsilon_D}}\,dE_s E_i^* \frac{e^{-i\Delta kL}-1}{-i\Delta k}. \end{aligned} \tag{6.2}$$

Thus, the output intensity of the resulting difference frequency output is obtained as follows.

$$\mathrm{I}_D = \frac{1}{2}\left(\frac{\mu}{\varepsilon_0}\right)^{3/2}\frac{\omega_D^2 L^2 d^2}{n_D n_s n_i}\mathrm{I}_s\mathrm{I}_i\mathrm{sinc}^2\left(\frac{\Delta kL}{2}\right), \tag{6.3}$$

where ω_D is the difference frequency, I_s (I_i) is the intensity of the signal (idler) output, and

n_D, n_s, and n_i represent the corresponding refractive indices, respectively. Equation (6.4) also represents the output energy of the difference frequency under the phase matching ($\Delta k = 0$).

$$\mathrm{E}_D = \frac{1}{2}\left(\frac{\mu}{\varepsilon_0}\right)^{3/2} \frac{\omega_D^2 L^2 d^2}{n_D n_s n_i} \mathrm{E}_s \mathrm{E}_i \frac{A_D}{A_s \cdot A_i} T_D T_s T_i, \tag{6.4}$$

where E_s (E_i) is the incident energy of the signal (idler) output, and A_D, A_s, and A_i are the mode field areas of the difference frequency, signal, and idler outputs, respectively. T_D, T_s, and T_i are the surface power transmittance at the difference frequency, signal, and idler outputs, respectively. Considering the absorption effects for the crystal,[1)] eq. (6.4) can be extended as follows.

$$\begin{aligned}\mathrm{E}_D = \frac{1}{2}\left(\frac{\mu}{\varepsilon_0}\right)^{3/2} \frac{\omega_D^2 L^2 d^2}{n_D n_s n_i} \mathrm{E}_s \mathrm{E}_i \frac{A_D}{A_s \cdot A_i} T_D T_s T_i e^{-\alpha_D L} \\ \cdot \frac{1 + e^{-\Delta\alpha L} - 2e^{-\Delta\alpha L/2}}{(\Delta\alpha L/2)^2}\end{aligned} \tag{6.5}$$

$\Delta\alpha$ is $\alpha_s + \alpha_i - \alpha_D$, where α_s, α_i, and α_D are the absorption coefficients of the crystal against the signal, idler, and difference frequency outputs, respectively.

The signal and idler carries the topological charges ℓ_s and ℓ_i.

$$E_{s,i} = u_{s,i}(r)\exp[i(\ell_{s,i}\phi - \omega_{s,i}t)] \tag{6.6}$$

And then, the difference frequency output will be given as follows:

$$\begin{aligned}E_D \propto \exp\{i[(\ell_s - \ell_i)\phi - |\omega_s - \omega_i|t]\}\ ;(\omega_s > \omega_i), \\ \exp\{i[(\ell_i - \ell_s)\phi - |\omega_s - \omega_i|t]\}\ ;(\omega_i > \omega_s).\end{aligned} \tag{6.7}$$

Therefore, the following relation is established.

$$\ell_D = \frac{(\omega_s - \omega_i)}{|\omega_s - \omega_i|}(\ell_s - \ell_i) \tag{6.8}$$

Equation (6.8) can be rewritten in terms of the wavelength.

$$\ell_D = -\frac{(\lambda_s - \lambda_i)}{|\lambda_s - \lambda_i|}(\ell_s - \ell_i) \tag{6.9}$$

In this chapter's work, the topological charge of the signal and idler outputs are 1 and 0, respectively, regardless of the lasing wavelength. Thus, the topological charge of the resulting difference frequency output is determined by the magnitude relation of lasing wavelengths between the signal and idler.

6.2 Experimental setup

Figure 6.1 shows a diagram of the mid-infrared tunable optical vortex source. The system is mainly composed of an optical parametric oscillator (OPO) and a difference frequency generator (DFG). The OPO cavity is formed of a concave (curvature radius, 2000 mm) input mirror with high reflectivity (HR) for 2 μm and high transmittivity (HT) for 1 μm and a flat output coupler with ~80 % reflectivity for 2 μm and HT for 1 μm, in which two cascaded $KTiOPO_4$ (KTP) crystals {12×9×27 mm^3, θ = 53° to *z*-axis, anti-reflection coating in a wavelength range of 1-2.6 μm, type-II phase matching [ordinary wave (pump) → ordinary wave (signal) + extraordinary wave (idler)]} are located with opposite orientations each other. Such a geometric arrangement enables the collinearly generation of the signal and idler outputs without a lateral displacement of the idler originated from the walk-off effects of the KTP crystal.

The pumping source for the OPO is a Q-switched Nd:YAG laser (lasing wavelength, 1.06 μm; pulse duration, ~25 ns; pulse repetition frequency, 50 Hz). The laser output with a Gaussian mode is transformed to be a 1st-order vortex beam with a topological charge of ℓ =1 by use of a spiral phase plate, and is carried to the KTP crystals (beam diameter on the crystal, ~0.78 mm). The wavelengths of the resulting signal and idler outputs are also tuned by rotating the KTP crystals with the Galvano stages.

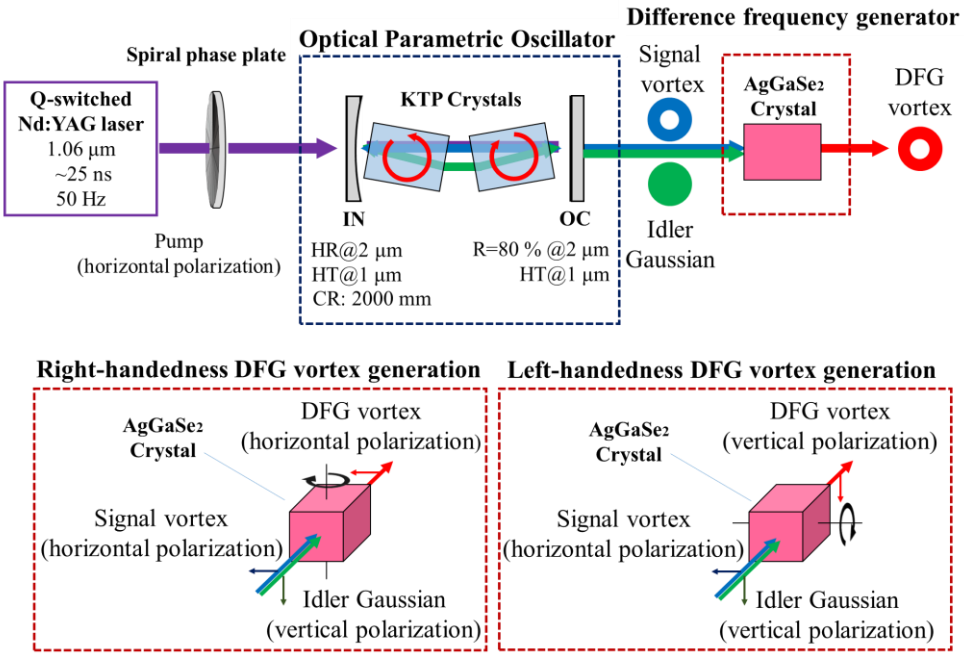

Fig. 6.1 Schematic diagram of the ultra-widely tunable optical vortex generation system.

Note that this OPO system always produces the signal output with a vortex mode (ℓ_s = 1) and the idler output with a Gaussian mode (ℓ_i = 0), respectively, due to the walk-off effects of the KTP crystal, [2,3] as mentioned in section 4.8.

After divided from the pump beam (i.e. un-frequency converted pump beam) by using a dichroic mirror (HR for 1 μm and HT for 2 μm), the vortex signal and Gaussian idler outputs generated from the OPO are directly delivered to a $AgGaSe_2$ (AGS) crystal (10×10×20 mm^3, θ = 56.95° to z-axis, type-II phase matching) used for the DFG. The AGS crystal angle is also tuned to the appropriate phase matching angle at the difference frequency.

The topological charge, ℓ_D, of the resulting difference frequency output is governed by eq. (6.9). When $\lambda_s < \lambda_i$, the difference frequency output will exhibit the same topological charge (ℓ_D = 1) as that of the signal. By swapping the lasing wavelengths of the signal and idler ($\lambda_s > \lambda_i$), the handedness (the sign of the topological charge) of the difference frequency output will be inverted (ℓ_D = -1). The optical axis of the AGS crystal is then rotated by 90 degrees around the beam propagation axis so as to establish the phase matching condition.

The spatial forms and wavefronts of the signal, idler, and difference frequency output are observed by a pyroelectric camera in combination with a laterally self-referenced interferometer (Mach-Zehnder interferometer). A germanium (Ge) filter which absorbs the undesired 1 μm pump beam and 2 μm signal/idler output is also utilized to obtain only the difference frequency output.

6.3 Experimental results and discussion

The spatial forms and wavefronts of the pump, signal, and idler are summarized in Fig. 6.2. The signal output carried the same 1st-order optical vortex mode with a topological charge of 1 as the pump, evidenced by a pair of downward and upward Y-formed fringes [Figs. 6.2(a)-(d)]. On the other hand, the idler output was then produced as a Gaussian mode with no phase singularity [Figs. 6.2(e) and (f)], so as to satisfy the conservation of the orbital angular momentum among the pump, signal, and idler.

As shown in Fig. 6.3, the vortex signal and Gaussian idler outputs were observed in a wavelength range of 1.78-2.71 μm. Figure 6.4 also shows the output energies transfer of the signal (1.97 μm) and idler (2.32 μm) against the pump energy. The maximum pulse energies of 3.9 mJ (1.9 mJ) for the signal (idler) was measured when a pump energy of 30 mJ was injected. The lasing threshold was then approximately 8 mJ.

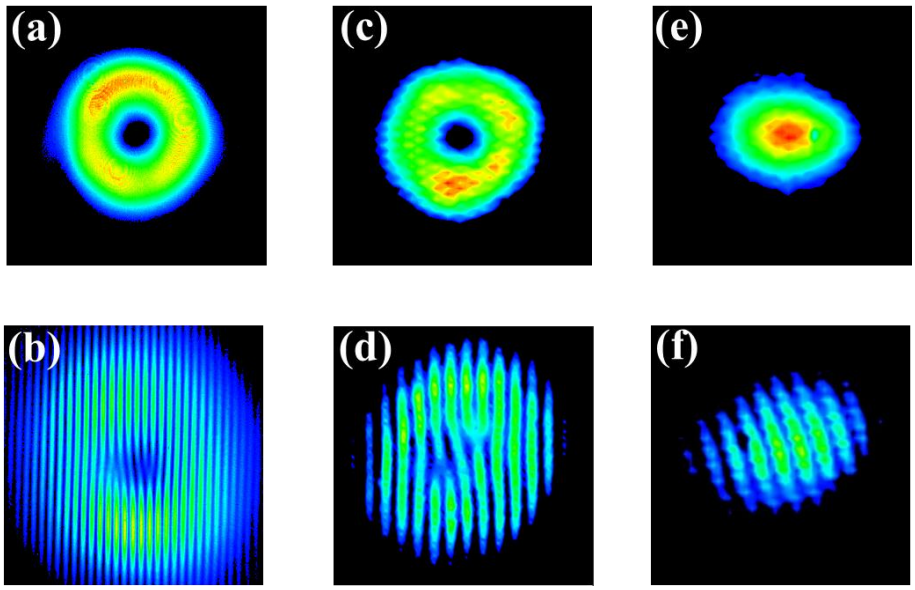

Fig. 6.2 (a) Spatial profiles and (b) wavefronts of the pump (1.06 μm). (c) Spatial profiles and (d) wavefronts of the signal (1.97 μm). (e) Spatial profiles and (f) wavefronts of the idler (2.32 μm).

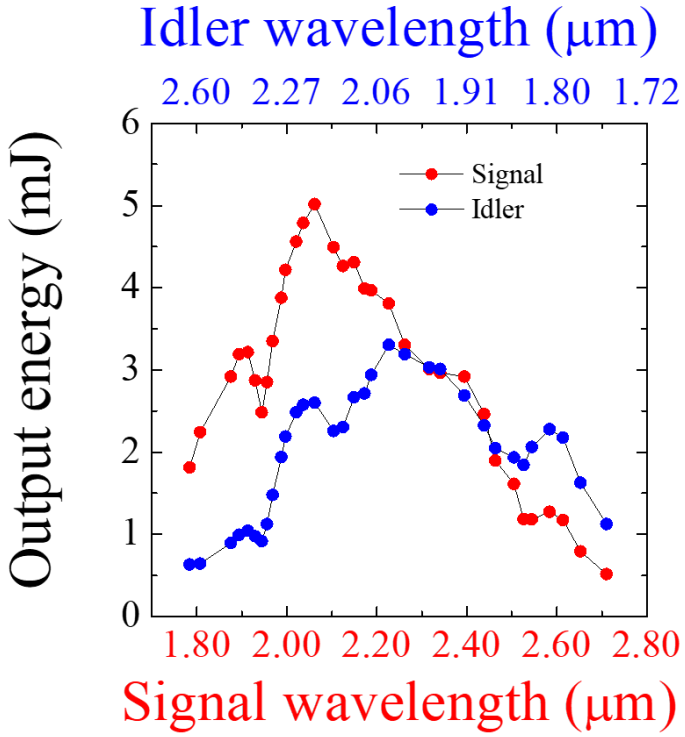

Fig. 6.3 Tunabilities of the vortex signal (red) and the Gaussian idler (blue).

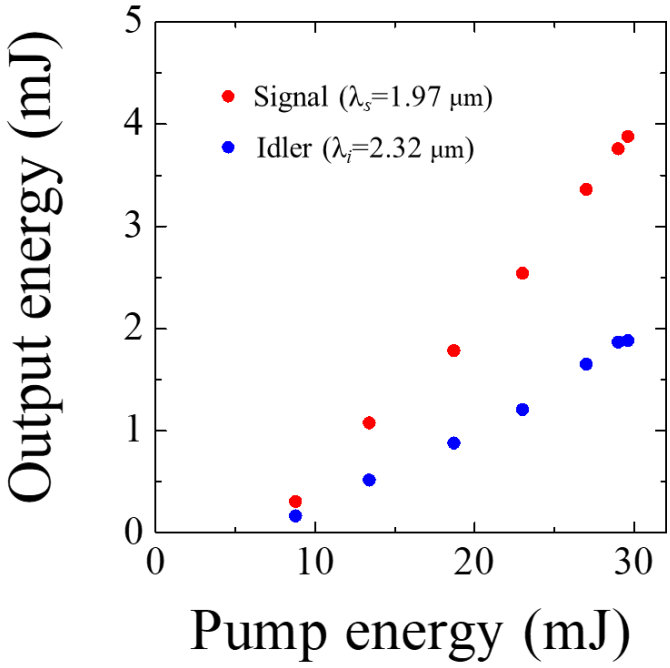

Fig. 6.4 Output pulse energies of the vortex signal (1.97 μm) and the Gaussian idler (2.32 μm) at various pump energies.

When the vortex signal (1.97 μm) and the Gaussian idler (2.32 μm) outputs were collinearly directed to the AGS crystal, the difference frequency output with an annular spatial mode was obtained [Fig. 6.5(a)]. The wavefront also exhibited a pair of downward and upward Y-formed fringes [Fig. 6.5(b)], denoting a 1st-order optical vortex with a topological charge of 1. The handedness (the sign of the topological charge) of the difference frequency output could be reversed by swapping the lasing wavelengths of the vortex signal and Gaussian idler (λ_s = 2.32 μm, λ_i = 1.97 μm), confirmed by the inverted orientation of Y-formed fringes (a pair of upward and downward Y-formed fringes) [Figs. 6.5(c) and (d)].

The tunabilities of the difference frequency vortex output with ℓ_D = 1 and -1 were 6-18 μm, which corresponds to so called "whole mid-infrared region", as shown in Figs. 6.6 and 6.7. Maximum energy of the difference frequency output with ℓ_D= 1 (-1) was measured to be 0.33 mJ (0.21 mJ) around 9 μm.

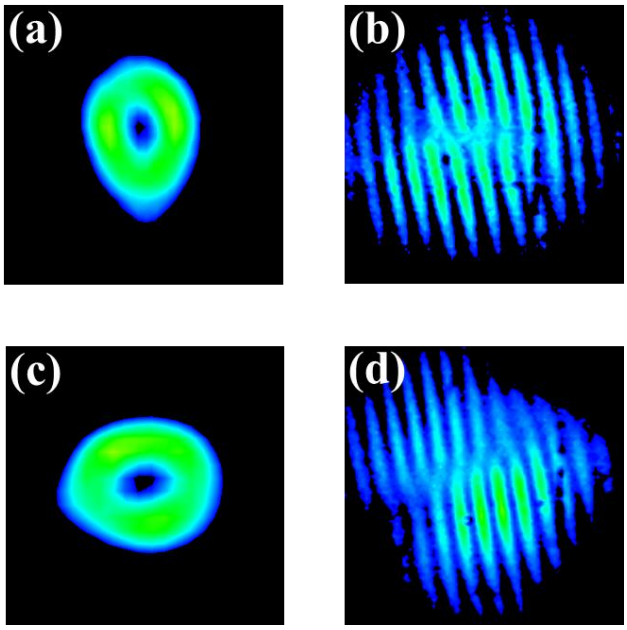

Fig. 6.5 (a) Spatial profile and (b) wavefront of the mid-infrared output (13 μm) produced from the DFG pumped by the vortex signal (1.97 μm) and the Gaussian idler (2.32 μm). (c) Spatial profile and (d) wavefront of the mid-infrared output (13 μm) from the DFG pumped by the vortex signal (2.32 μm) and the Gaussian idler (1.97 μm).

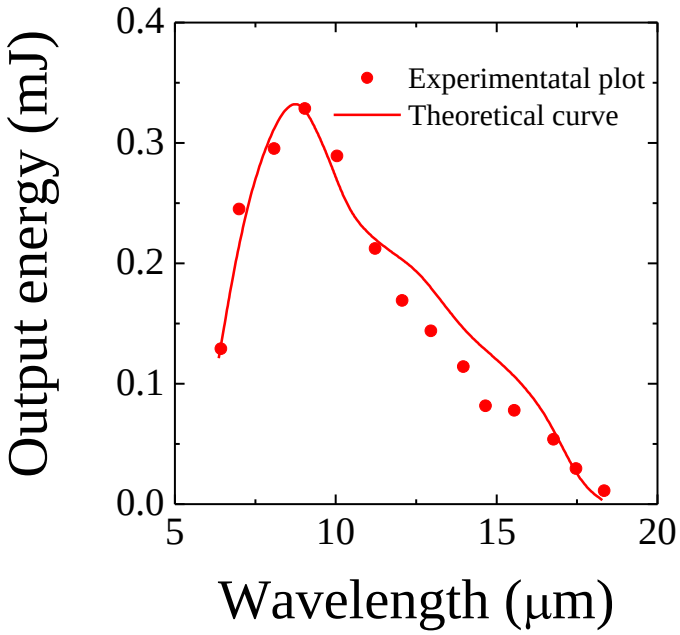

Fig. 6.6 Output energies of the mid-infrared optical vortex as a function of wavelengths with ℓ_D = 1. The solid line represents a theoretical curve.

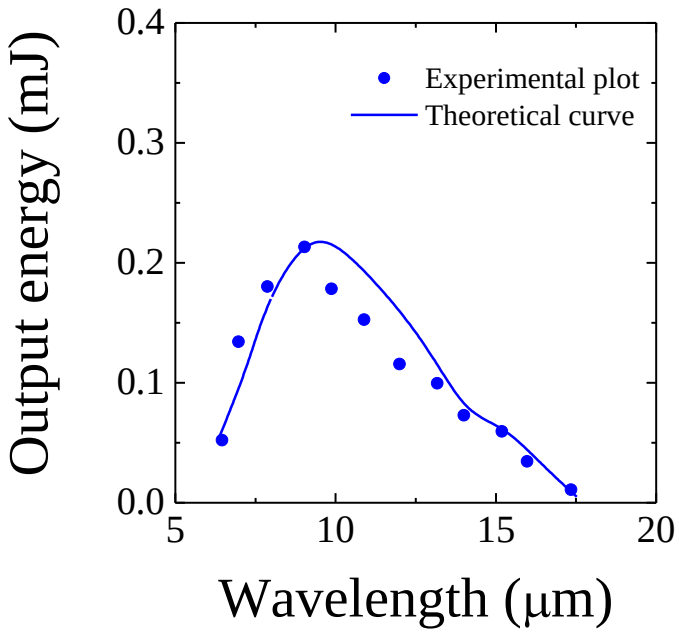

Fig. 6.7 Output energies of the mid-infrared optical vortex as a function of wavelengths with ℓ_D = -1. The solid line represents a theoretical curve.

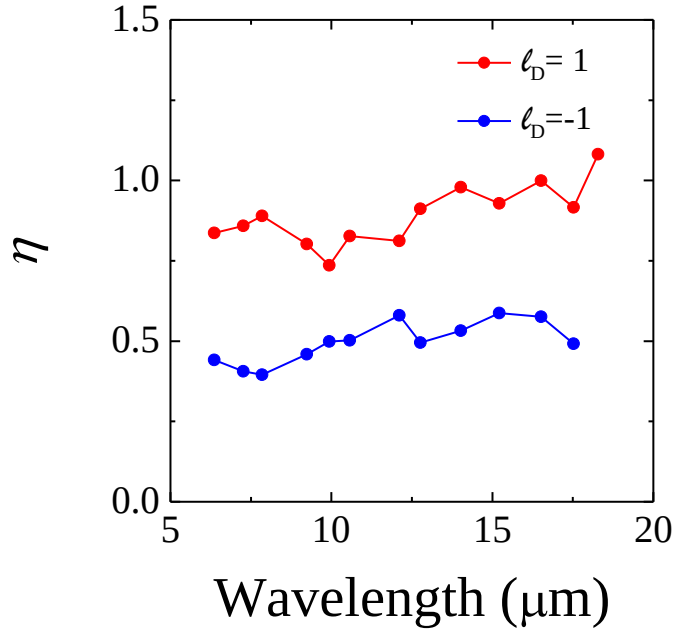

Fig. 6.8 Cross-section factor, η, as a function of difference frequencies.

The theoretical pulse energy, E_D, of the difference frequency output can be also estimated by eq. (6.5). The beam areas, A_D, A_s, and A_i, of the difference frequency, signal, and idler output, measured by the pyroelectric camera with 4-sigma method (ISO11146 standard), were then substituted for the equation. Figure 6.8 also shows the cross-section factor, η, defined as a ratio of cross-sectional area, given by $A_D/(A_s \cdot A_i)$, at various difference frequencies. The simulated curves of the difference frequency pulse energies (solid lines in Figs. 6.6 and 6.7) were good agreement with the experimental plots, regardless of the handedness of the difference frequency output.

6.4 Conclusion

A tunable 'entire mid-infrared (6-18 μm)' vortex source based on a $AgGaSe_2$ difference frequency generator pumped by an optical vortex parametric oscillator has been presented. The handedness of the mid-infrared vortex output can be selectively controlled by swapping the lasing frequencies of the signal and idler outputs in combination with the 90 degrees rotation of optical axis of the $AgGaSe_2$ crystal.

Such ultra-widely tunable mid-infrared vortex sources will pioneer the new application of the material science, e.g. super-resolution molecular spectroscopy, i.e. assignment or excitation of both stretching and binding modes of the target molecules with high spatial resolution beyond the diffraction limit, and chiral polymeric materials fabrication without any destruction of chemical structures.

6.5 References

1) P. P. Bey, J. F. Giuliani, and H. Rabin, "Generation of a Phase-Matched Optical Third Harmonic by Introduction of Anomalous Dispersion into a Liquid Medium," Phys. Rev. Lett. **19**, 819 (1967).
2) T. Yusufu, Y. Tokizane, M. Yamada, K. Miyamoto, and T. Omatsu, "Tunable 2-μm optical vortex parametric oscillator," Opt. Express **20**, 23666 (2012).
3) T. Yusufu, Y. Tokizane, K. Miyamoto, and T. Omatsu, "Handedness control in a 2-μm optical vortex parametric oscillator," Opt. Express **21**, 23604 (2013).

Chapter 7 – Conclusions

7.1 Thesis summary

I have demonstrated the tunable optical vortex generation with ultra-broadband tunability from visible to mid-infrared region by employing an optical parametric oscillator and a difference frequency generator. The key results in this work are summarized.

First, a tunable optical vortex laser with extremely wide tunability “over a 2-octave band”, comprised of an optical vortex pumped LiB_3O_5 optical parametric oscillator, has been developed. This system provides optical vortices with a pulse energy of >0.1 mJ in a wavelength range of 0.67-2.57 μm. This tunability, to the best of our knowledge, is the widest in the optical vortex laser constructed by a single optical resonator. Furthermore, a new basis for controlling the topological charge in the optical parametric oscillator (based on the spatial amplitude overlap integral between the pump and signal beams) has been presented in this work. This method enables us to produce the optical vortex with versatile topological charge in the range of -1 to 2, including an up-converted topological charge, i.e. a vortex output with a higher topological charge than that of the pump beam.

Second, a tunable ‘entire mid-infrared’ vortex source based on a $AgGaSe_2$ difference frequency generator pumped by an optical vortex pumped $KTiOPO_4$ optical parametric oscillator has been demonstrated. Its tunability covers the wavelength range of 6-18 μm, called as ‘molecular finger print’, which includes stretching and binding modes of the various molecules.

Such ultra-broadband optical vortex sources will lead the development of the new optical vortex application, such as super resolution molecular spectroscopy and chiral structures processing in organic materials.

7.2 Future work _ extension of topological charge diversity

The optical parametric oscillator pumped by higher-order optical vortex, e.g. 2^{nd}-order optical vortex, will further extend a versatility of topological charge.

$$\eta_{\ell_s} = \int_0^\infty E_{pump}\, E^*_{signal} \cdot 2\pi r\, dr$$
$$\propto \int_0^\infty r^2 \exp\left(-\frac{r^2}{\omega_p^2}\right) \cdot r^{|\ell_s|} \exp\left(-\frac{r^2}{\omega_s^2}\right) \cdot 2\pi r\, dr \qquad (7.1)$$

Figure 7.1 shows the spatial overlapping efficiency, η_{ℓ_s}, of the normalized electric field amplitudes between the 2nd-order vortex pump beam and the signal output, given by eq. (7.1). When the cavity length is less than 65 mm, η_3 exceeds η_1 and η_2, and thus the parametric cavity with such a length will produce a 3rd-order vortex mode ($\ell_s = 3$) as the signal. The idler will then carry a -1st-order vortex mode ($\ell_i = -1$), so as to conserve the OAM of the pump beam. Within a cavity-length of 65-160 mm, in which η_2 is more than η_1 and η_3, the cavity will be expected to yield a 2nd-order vortex signal ($\ell_s = 2$) and a Gaussian idler ($\ell_i = 0$), respectively. A further extended cavity with a length of > 160 mm ($\eta_1 > \eta_2, \eta_3$) will also generate a 1st-order vortex mode ($\ell_s = \ell_i = 1$) as the signal and idler outputs. Therefore, the optical vortices generation with versatile topological charge in the range of -1 to 3 (5 states) will be possible.

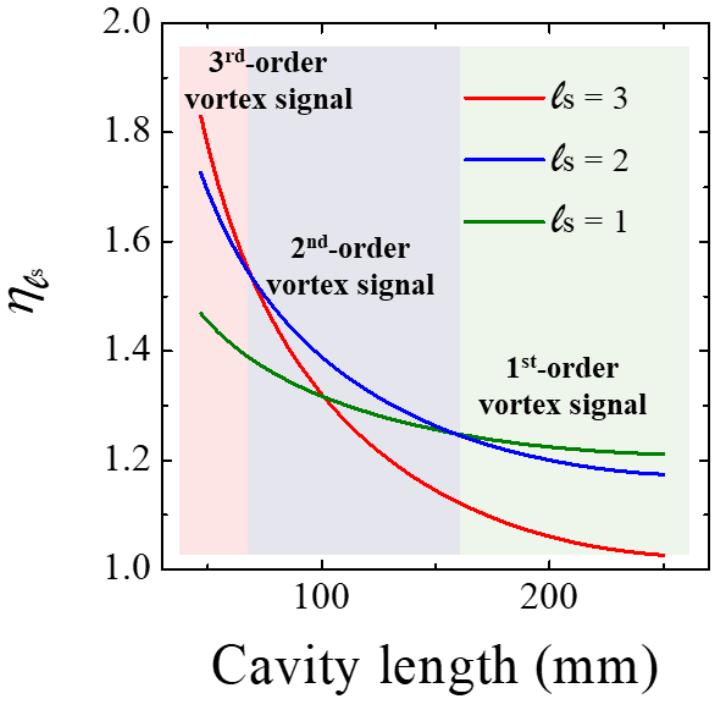

Fig. 7.1 Spatial amplitude overlapping efficiency of the electric fields between the 2nd-order vortex pump beam and the signal output at various cavity lengths.

7.3 Future work _ 3-5 μm optical vortices generation

In this thesis, I demonstrated the optical vortex generation in visible to mid-infrared region (0.67-18 μm), in which, however, there is a frequency gap in a range of 3-5 μm. The gap will be filled in by the optical parametric oscillator utilizing a periodically poled lithium niobate (PPLN) crystal. The PPLN is a designed, quasi phase-matched material, where the orientation of the dipole is periodically inverted (Fig. 7.2), which enables to provide a very large effective nonlinear coefficient. The poling period Λ is also determined by the following equation.

$$m\frac{2\pi}{\Lambda} = k_{pump} - k_{signal} - k_{idler}, \tag{7.2}$$

in which m is arbitrary integer, and k_{pump}, k_{signal}, and k_{idler} are the wave number of the pump, signal, and idler beams. A 1 μm optical vortex pumped PPLN (Λ ~30 μm) optical parametric system, formed of a singly resonant cavity for the signal (wavelength range, 1.65-1.35 μm), will provide the tunable optical vortex as the idler in the range of 3.0-5.0 μm by varying the temperature of the crystal.

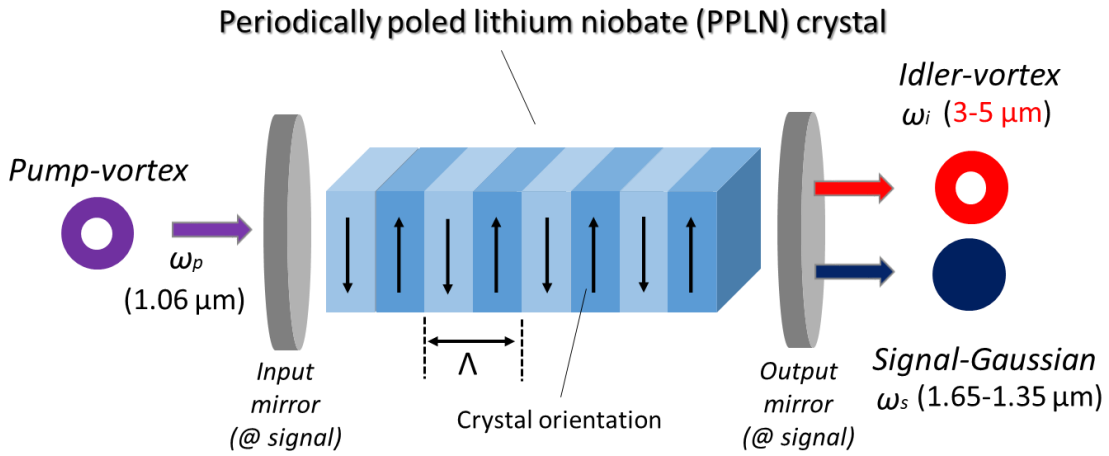

Fig. 7.2 Schematic diagram of optical parametric oscillator to generate 3-5 μm optical vortex.

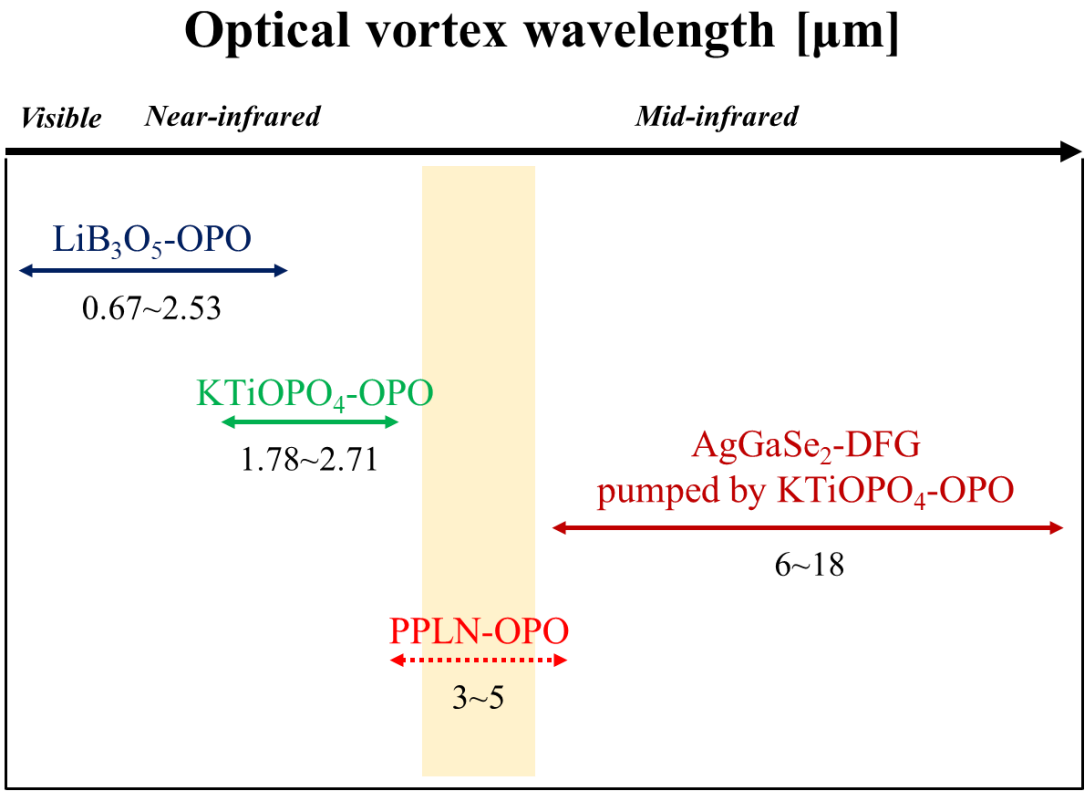

Fig. 7.3 Tunabilities of the optical vortex generated from various configurations.

Appendix

A.1 Interferometric fringes

The topological charge, of the vortex output from the optical parametric oscillator was investigated by measurement of the self-referenced interferometric fringes. When a 1st-order optical vortex beam, $E_V(x,y) = u_V(x,y)\exp\{i[-k_z z + \phi(x,y)]\}$, is overlaid by itself with an angle of 2θ $[= 2\tan^{-1}(k_x/k_z)]$ (see Fig. a.1), the resulting interferometric patterns exhibit a pair of downward (upward) and upward (downward) fork fringes, according to eq. (a.1).

$$\begin{aligned} I &= |E_V(x+a,y)\exp(+ik_z\theta x) + E_V(x-a,y)\exp(-ik_z\theta x)|^2 \\ &= |u_V(x+a,y)|^2 + |u_V(x-a,y)|^2 \\ &\quad -2\,u_V(x+a,y)u_V(x-a,y) \\ &\quad \cdot\cos[\phi(x-a,y) - \phi(x+a,y) - 2k_z\theta x] \end{aligned} \tag{a.1}$$

Figures a.2(a) and (b) represent the simulated interferometric fringes for 1st-order and -2nd-order optical vortices, respectively. The number of branches corresponds to the magnitude of topological charge, e.g. optical vortices with a topological charge of $|\ell|$ produce a pair of fork fringes with $|\ell| + 1$ branches, and then the orientations of the forks are also determined by the sign of the topological charge.

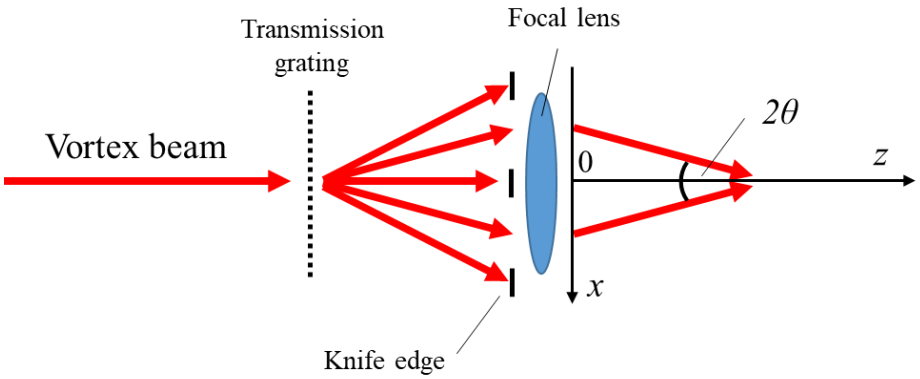

Fig. a.1 Self-referenced interferometric technique.

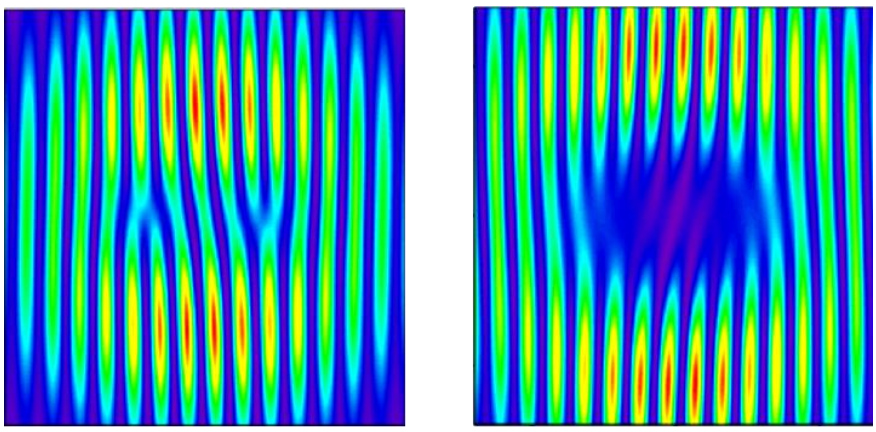

Fig. a.2 Simulated self-referenced interferometric patterns of optical vortices with a topological charge of (a) 1 and (b) -2, respectively.

A.2 M^2 factor

The factor, called as beam propagation factor, is often utilized to represent the beam quality of a laser beam. For example, the focal spot size of a higher-order laser beam is M times larger than that of a fundamental Gaussian beam (TEM_{00} mode) (Fig. a.3).

$$W_0 = M\omega_0, \tag{a.2}$$

where W_0 and ω_0 are the focal spot sizes of laser beams with the higher-order and the fundamental Gaussian modes, respectively.

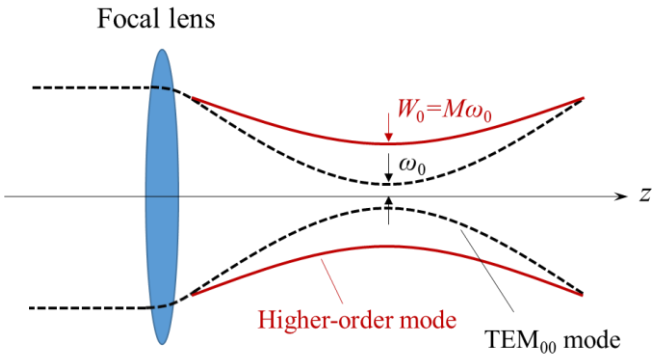

Fig. a.3 Diagram of beam propagation.

And then, the beam size of the higher-order laser beam can be rewritten as follows.

$$W(z) = W_0 \sqrt{1 + \left(\frac{\lambda z M^2}{\pi W_0^2}\right)^2} \tag{a.3}$$

Assuming $z \gg \pi W_0^2 / \lambda M^2$, eq. (a.3) becomes to eq. (a.4).

$$W(z) \simeq \frac{\lambda z M^2}{\pi W_0} \tag{a.4}$$

Therefore, the divergence angle of the beam can be expressed as

$$\theta = \frac{W(z)}{z} = \frac{\lambda M^2}{\pi W_0}. \tag{a.5}$$

Furthermore multiplying both sides of the above-mentioned equation by W_0, eq. (a.5) is

$$W_0 \theta = M^2 \frac{\lambda}{\pi}. \tag{a.6}$$

The left side of this equation is defined as beam parameter product (BPP) and M^2 in the right side is beam quality factor.

A.3 Spectral linewidth measurement

A spectral linewidth of the pumping laser was discussed by the fringe visibility of interferogram at various optical path length differences.[1)] When two laser beams interfere with the path length difference of l (Fig. a.4), the intensity of the interferometric pattern can be expressed below.

$$I = I_1 + I_2 + 2\sqrt{I_1 I_2} \cdot \gamma(l) \cdot \cos kx, \tag{a.7}$$

where $\gamma(l)$ is the mutual coherence function and satisfies the following relationship.

$$V(l) = \frac{I_{max} - I_{min}}{I_{max} + I_{min}} = \frac{2\sqrt{I_1 I_2}}{I_1 + I_2} \cdot \gamma(l), \tag{a.8}$$

in which $V(l)$ is called as the fringe visibility. I_{max} and I_{min} are also maximum and minimum intensities of the interferometric fringes.

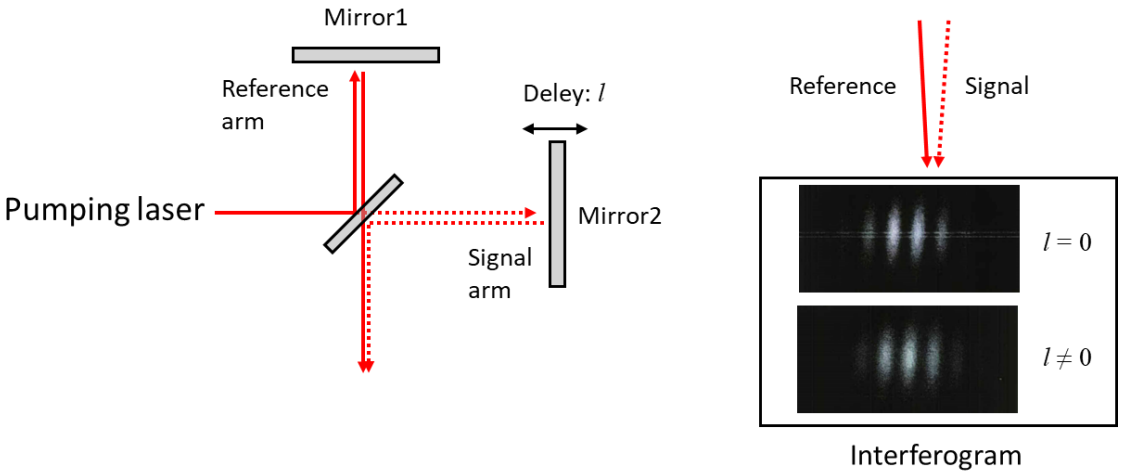

Fig. a.4 Fringe visibility measurement by Michelson interferometer.

Such a two-beam interference measurement can obtain the interferometric fringes if the delay is less than coherence length, l_c.

$$l_c = c\tau_c, \tag{a.9}$$

where τ_c is often defined as coherence time.

Also, the coherence function, $\gamma(l)$, can be regarded as an autocorrelation function. According to the Wiener-Khintchine's theorem, the relationship of the Fourier transformation is also established between the power spectrums (i.e. spectrum densities) and autocorrelation functions. Therefore, the coherence time of the laser corresponds to inverse of the spectrum linewidth:

$$\tau_c = \frac{2\pi}{\Delta\omega} = \frac{1}{\Delta f}. \tag{a.10}$$

References

1) A. Yariv, P. Yeh, *Photonics: Optical Electronics in Modern Communications* (Oxford University Press, New York, 2007) 6th ed., p.491.